A stable microtubule bundle formed through an orchestrated multistep process controls quiescence exit

Damien Laporte[1]*, Aurélie Massoni-Laporte[1], Charles Lefranc[1], Jim Dompierre[1], David Mauboules[1], Emmanuel. T. Nsamba[2], Anne Royou[1], Lihi Gal[3], Maya Schuldiner[3], Mohan L. Gupta Jr[2], Isabelle Sagot[1]

Affiliation :

1: Univ. Bordeaux, CNRS, IBGC, UMR 5095, Bordeaux, France

2: Genetics, Development, and Cell Biology, Iowa State University, Ames, IA 50011, USA.

3: Department of Molecular Genetics, Weizmann Institute of Science, Rehovot, Israel

* Corresponding author: Damien.laporte@ibgc.cnrs.fr

Abstract

Cells fine-tune microtubule assembly in both space and time, to give rise to distinct edifices with specific cellular functions. In proliferating cells, microtubules are highly dynamics, and proliferation cessation often leads to their stabilization. One of the most stable microtubule structures identified to date is the nuclear bundle assembled in quiescent yeast. In this report, we characterize the original multistep process driving the assembly of this structure. This Aurora B-dependent mechanism follows a precise temporality that relies on the sequential actions of kinesin-14, kinesins-5 and involves both microtubule-kinetochore and kinetochore-kinetochore interactions. Upon quiescence exit, the microtubule bundle is disassembled via a cooperative process involving kinesin-8 and its full disassembly is required prior to cells re-entry into proliferation. Overall, our study provides the first description, at the molecular scale, of the entire life cycle of a stable microtubule structure *in vivo*, and sheds light on its physiological function.

Introduction

Microtubules (MTs) are hollow cylindrical polymers assembled by the non-covalent interaction of α- and β-tubulin heterodimers. MTs are generally nucleated at MT organizing centers (MTOC) by a ɣ-tubulin complex (ɣ-TuC) which acts as a template and stabilizes the so-called MT "minus-end" (Liu et al., 2021; Roostalu and Surrey, 2017; Sanchez and Feldman, 2017; Thawani and Petry, 2021). At the opposite end, the "plus-end" (+end), MTs elongate by the addition of GTP tubulin. The β-tubulin bound GTP is hydrolyzed and stable but transient GDP + Pi intermediates are generated in the region immediately behind the growing +end. Subsequent Pi release favors MT depolymerization which can be rescued by *de novo* GTP-tubulin addition (Cleary and Hancock, 2021; Gudimchuk and McIntosh, 2021). Thus, MTs alternate between periods of growth and shrinkage, a behavior termed dynamic instability (Mitchison and Kirschner, 1984). *In vivo*, a profusion of MT-associated proteins (MAPs) regulate MT length and dynamics (Bodakuntla et al., 2019; Goodson and Jonasson, 2018). In addition, MTs are often assembled from multiple tubulin variants or isotypes, and are modified by a cohort of post-translational modifications that modulate MT dynamics directly or by influencing the recruitment of MAPs (Janke and Magiera, 2020; Roll-Mecak, 2020). Other MAPs organize MTs into high-ordered assemblies, either by cross-linking MTs or by connecting them with cellular structures such as membranes, chromosomes or actin cytoskeleton components (Bodakuntla et al., 2019; Meiring et al., 2020). Cells fine-tune these mechanisms in both space and time to give rise to distinct MT edifices with specific functions.

In proliferating cells, MT dynamics are crucial for their functions. It allows exploration of the cell volume in search of structures to "capture", such as centromeres during mitosis, or to exert pushing or pulling forces required for various cellular processes such as cell migration or morphogenesis (Heald and Khodjakov, 2015; Kirschner and Mitchison, 1986). The MT

58 cytoskeleton can undergo extensive rearrangements and assemble more stable MT
59 structures, especially when cells change fate (Meiring et al., 2020; Röper, 2020). For example,
60 in terminally differentiated cells, such as epithelial cells, cardiomyocytes or neurons, stable
61 MT networks make up the majority, and ensure critical cellular functions such as cell shape
62 maintenance or long-distance intracellular transport (Baas et al., 2016; Muroyama and
63 Lechler, 2017). Defects in MT stabilization are at the origin of many human pathologies,
64 including neurodegenerative diseases and ciliopathies (Anvarian et al., 2019; Wheway et al.,
65 2018). Effectors responsible for MT stabilization have been actively searched for since the
66 1980's. In mammals, the involvement of specific MAPs such as Tau, MAP2, MAP6 and PRC1,
67 or tubulin post-translational modifications has been extensively studied. While their
68 contributions to MT stabilization are central and undisputed, their sole actions do not fully
69 explain the observed levels of MT stability in many types of non-dividing cells (Hahn et al.,
70 2019).

71 For years, yeast species have been instrumental in unraveling mechanisms that
72 regulate MT dynamics in eukaryotes. While proliferating yeast cells exhibit a dynamic MT
73 network (Winey and Bloom, 2012), proliferation cessation goes with the formation of
74 dramatically stable MT structures in both *S. cerevisiae* and *S. pombe* (Laporte and Sagot, 2014;
75 Laporte et al., 2013, 2015). Upon quiescence establishment, *S. cerevisiae* cells assemble a
76 bundle composed of stable parallel MTs, hereafter referred to as the Q-nMT bundle, for
77 Quiescent-cell nuclear Microtubule bundle. This structure originates from the nuclear side of
78 the spindle pole body (SPB), the yeast equivalent of the centrosome. It spans the entire
79 nucleus and relocalizes kinetochores and centromeres, which remain attached to MT +ends
80 (Laporte and Sagot, 2014). Because the MTs embedded in the Q-nMT bundle are not all of the
81 same length, the structure has a typical arrow shape. When cells exit quiescence, the Q-nMT

82 bundle depolymerizes and, by pulling the attached centromeres back to the SPB, allows the
83 recovery of the typical Rabl-like configuration of chromosomes found in G1 yeast cells (Jin et
84 al., 1998). The molecular mechanisms underlying the formation of this peculiar stable MT
85 structure and its physiological function(s) are not understood. However, cells defective in Q-
86 nMT bundle formation have a compromised survival in quiescence and a drastically reduced
87 fitness upon cell cycle re-entry (Laporte and Sagot, 2014; Laporte et al., 2013, 2015).

88 Here, we show that Q-nMT bundle formation is a multistep process that follows a
89 precise temporal sequence. The first step relies on Aurora B/Ipl1 activity and requires the
90 kinesin-14 Kar3, its regulator Cik1, and the EB1 homolog Bim1. It leads to the formation of a
91 short (≈ 1 µm) and stable bundle that resembles a half mitotic spindle. Importantly, in this first
92 step, MT polymerization and stabilization are coupled. In a second step, additional MTs
93 polymerize from the SPB, elongate, and are zipped to pre-existing MTs in a Cin8/kinesin-5
94 dependent manner. Complete stabilization of the Q-nMT bundle is achieved in a third and
95 final step that requires the kinesin-5 Kip1. Our observations further indicate that Q-nMT
96 bundle assembly requires both MT-kinetochore attachment and inter-kinetochore
97 interactions. Finally, we show that, upon exit from quiescence, the Q-nMT bundle
98 disassembles from its +ends, each MT depolymerizing in coordination with its neighbors, via
99 the action of the depolymerase Kip3, a member of the kinesin-8 family. Importantly, we show
100 that the complete disassembly of the Q-nMT bundle is required for cells to re-enter the
101 proliferation cycle. Overall, this study describes the entire life cycle of a MT structure, from
102 the molecular mechanisms involved in its formation and stabilization to its disassembly and
103 further suggests that this atypical quiescent specific structure could act as a regulator, or a
104 “control point” for cell cycle resumption upon exit from quiescence.

105 ## Results

106 **The Q-nMT bundle formation is a three-step process.**

107 We have previously shown that the Q-nMT bundle observed in quiescent cells is a
108 stable nuclear structure (Laporte et al., 2013). To investigate whether the stabilization of the
109 Q-nMT bundle was concomitant with its assembly or whether it assembled first as a dynamic
110 structure and then gets stabilized, we quantified the Q-nMT bundle length (Fig. 1A) and
111 thickness (Fig. 1B) upon quiescence establishment following carbon source exhaustion. We
112 found that the Q-nMT bundle assembly process could be divided into 3 sequential phases. In
113 an initial phase (phase I), MTs elongated from the SPB to reach ≈ 0.8 µm. The number of these
114 MTs, referred to as phase I-MTs, was approximately the same as in a mitotic spindle (see inset
115 of Fig. 1B and Sup. Fig. 1A). Importantly, phase I-MTs were resistant to nocodazole (Noc), a
116 MT poison that causes dynamic MT depolymerization, indicating that phase I-MT stabilization
117 was concomitant with their polymerization (Fig. 1A-B). In a second phase, beginning ≈ 10h
118 after glucose exhaustion, additional MTs emerged from the SPB (phase II-MTs) and elongated
119 along phase I-MTs, nearly doubling the thickness of the phase I MT bundle (Fig. 1B and Sup
120 Fig. 1A). At this stage, the tip of the newly elongated MTs were unstable (Fig. 1A-B). Complete
121 stabilization of the Q-nMT bundle was achieved ≈ 48h after glucose exhaustion (phase III).
122 Indeed, after this step, a Noc treatment did not affect either the length or the thickness of the
123 Q-nMT bundle (Fig. 1A-B and Sup. Fig. 1B). Plotting Q-nMT bundle width as a function of length
124 for each individual cell before and after Noc treatment further revealed the 3 successive
125 phases of the Q-nMT bundle formation (Fig. 1C). Of note, Q-nMT bundles were also observed
126 both in diploid cells upon glucose exhaustion (Sup. Fig. 1C) and in haploid cells transferred to
127 water (Sup. Fig. 1D).

128 To confirm the above observations, first, we followed Nuf2-GFP, a protein that localizes
129 to the MT +end. As expected, movies showed that upon Q-nMT bundle formation initiation,
130 the Nuf2-GFP signal relocated from the SPB to the distal part of elongating Q-nMT bundles
131 (Sup. Fig. 1E). In phase II, when cells were treated with Noc, the Nuf2-GFP signal followed
132 depolymerizing MTs (Fig. 1D, left panel), testifying for the instability of phase II-MTs. In
133 contrast, the Nuf2-GFP signal remained immobile upon Noc treatment in phase III, as cells
134 have fully stabilized Q-nMT bundles (Fig. 1D, right panel). Second, we measured the γ-tubulin
135 (Tub4) signal at the SPB and found that Tub4 started to accumulate at the SPB at the beginning
136 of phase I to reach a plateau at the end of phase II (Fig. 1E and Sup. Fig. 1F). Interestingly, the
137 amount of Tub4 at the SPB was proportional to the thickness of the Q-nMT bundle (Sup. Fig.
138 1G). Finally, in order to confirm the two waves of MT elongation, we developed a strain
139 expressing mTQZ-Tub1 from the endogenous TUB1 promoter and mRuby-TUB1 under the
140 ADH2 promoter, a promoter that is de-repressed after glucose exhaustion, as confirmed by
141 western blot (Sup. Fig. 1H). We observed that mRuby-TUB1 was incorporated into the Q-nMT
142 bundle only after phase I (Fig. 1F and Sup. Fig. 1H) confirming the existence of a second wave
143 of MT elongation during phase II. All the above experiments led us to propose the model
144 shown in figure 1G.
145
146 **Q-nMT bundle formation is an essential time-regulated process.**
147 Increasing cytoplasmic viscosity has been shown to dampen MT dynamics (Molines et
148 al., 2022). Upon quiescence establishment, yeast cells undergo a transition from a fluid to a
149 solid-like phase (Munder et al., 2016; Joyner et al., 2016) and an acidification (Jacquel et al.,
150 2021) which could contribute to the formation of the Q-nMT bundle. Several lines of evidence
151 suggest that these changes in physicochemical properties are not involved in Q-nMT

152 formation. First, 4-day-old quiescent cells can simultaneously display both dynamic
153 cytoplasmic MTs (cMTs) and a stable Q-nMT bundle (Sup. Fig. 1I and (Laporte et al., 2013)).
154 Second, when we mimicked a fluid to solid-like phase transition in proliferating cells by
155 artificially lowering the pH, no stable MTs were observed, whereas F-actin aggregation was
156 induced (Sup. Fig. 1J) as expected (Peters et al., 2013). Third, 2-day-old quiescent cells
157 exhibiting a phase III Q-nMT bundle were able to grow *de novo* dynamic cMTs after a pulse-
158 chase Noc treatment (Sup. Fig. 1K).

159 Importantly, if Q-nMT bundle formation was solely dependent on physicochemical
160 changes, this structure should be able to assemble in late quiescence. By treating cells with
161 Noc upon glucose exhaustion, we were able to prevent the formation of the Q-nMT bundle in
162 early quiescence (Fig. 1H). Strikingly, when the drug was washed out, no Q-nMT bundle
163 assembled, even 144h after Noc removal (Fig. 1H). These cells had entered quiescence
164 because they had assembled actin bodies (Fig. 1H, right panel), another quiescent cell specific
165 structure (Sagot et al., 2006). This experiment strongly suggests that Q-nMT formation is a
166 process induced by a transient signal emitted upon glucose exhaustion.

167 We have previously shown that mutants unable to assemble Q-nMT bundles have
168 reduced viability in quiescence and a reduced ability to form colonies upon exit from
169 quiescence (Laporte et al., 2013). To establish a direct link between the absence of the Q-nMT
170 bundle and the above phenotypes, we took advantage of our ability to conditionally prevent
171 Q-nMT bundle formation in WT cells using Noc treatment at the onset of glucose exhaustion.
172 As shown in Sup. Fig. 1L, in the absence of the Q-nMT bundle, WT cells lose viability in
173 quiescence and survivors have a reduced ability to generate a progeny upon exit from
174 quiescence. In contrast, a similar Noc treatment of cells that have already assembled a stable
175 Q-nMT bundle (5-day-old cells) did not affect either the viability in quiescence or quiescence

176 exit efficiency, demonstrating that Noc did not have a toxic effect *per se*. Taken together, these
177 experiments confirm our initial findings that the Q-nMT bundle is important for both cell
178 survival during chronological aging and quiescence exit fitness.
179
180 **Steady state tubulin levels and Tub3 isotype are critical for Q-nMT bundle formation.**
181 We then focused on deciphering the molecular mechanisms involved in Q-nMT bundle
182 formation. Yeast cells express two α-tubulin isotypes, Tub1 and Tub3. In proliferating cells,
183 Tub1 constitutes the majority (Aiken et al., 2019; Nsamba et al., 2021; Schatz et al., 1986). In
184 4-day-old cells, the two α-tubulin isotypes were found embedded in the Q-nMT bundle. This
185 was observed using two different pairs of fluorescent proteins in order to avoid any influence
186 of the FP variants, and using both widefield and expansion microscopy (Fig. 2A and Sup. Fig.
187 2A). Since Tub3 stabilizes MTs *in vitro* (Bode et al., 2003), it may be key for Q-nMT bundle
188 formation. To test this hypothesis, we first analyzed the phenotype of *tub3Δ* cells. In phase II,
189 *tub3Δ* cells displayed short MT bundles that were sensitive to Noc. In phase III, no MT bundle
190 were detected (Fig. 2B and Sup. Fig. 2C). Thus, in this mutant, the MT bundles assembled
191 during phase I were not stable and eventually collapsed. In *tub3Δ* cells, the steady state
192 amount of α-tubulin is significantly reduced (Sup. Fig. 2B and (Nsamba et al., 2021)). Thus, the
193 amount of α-tubulin, but not Tub3 itself, may be important for Q-nMT bundle formation.
194 Indeed, mutants defective in α- and β-tubulin folding, such as the prefolding complex mutants
195 *pac10Δ*, *gim3Δ* or *yke2Δ,* or in tubulin heterodimer formation such as *pac2Δ*, or in β-tubulin
196 folding, such as *cin2Δ* or *cin4Δ*, all of which have a reduced amount of tubulin, were unable to
197 assemble a Q-nMT bundle (Sup. Fig. 2D-E).
198 To identify the role of Tub3 *per se*, we took advantage of the "*Tub1-only*" mutant, in
199 which the *TUB3* gene was replaced by the *TUB1* gene at the *TUB3* locus. This mutant expresses

200 only Tub1 and has an α-tubulin level similar to WT (Sup. Fig. 2B and (Nsamba et al., 2021)).
201 We found that "*Tub1-only*" cells have unstable Q-nMT bundles in phase II, and shorter, yet
202 stable, Q-nMT bundles in phase III (Fig. 2C and Sup. Fig. 2C). Moreover, "*Tub1-only*" Q-nMT
203 bundles were thinner than WT Q-nMT bundles (Fig. 2D). Taken together, our data indicate
204 that Tub3 is involved in MT elongation in phase II, since in the absence of this isotype, phase I
205 MT bundles could assemble and MT bundles could get stabilized in phase III, but the second
206 wave of MT nucleation and elongation was impaired as testified by thinner Q-nMT bundles in
207 both phase II and III.
208
209 **Kinetochores are critical for phase I but dispensable for the maintenance of Q-nMT bundles.**
210 Kinetochore components are enriched at the Q-nMT bundle +end ((Laporte et al.,
211 2013) and Sup Fig. 3A). We therefore tested whether kinetochore-MT attachment might play
212 a role in Q-nMT bundle formation. First, we disrupted kinetochore-MT attachment upon
213 glucose exhaustion using the well-established *ndc80-1* allele (Cheeseman et al., 2006; DeLuca
214 et al., 2018; Wigge et al., 1998). As shown in Fig. 3A, only very short MT structures were
215 detected in *ndc80-1* cells transferred to 37°C at the onset of quiescence entry, even after 4
216 days at non-permissive temperature (for control see Sup. Fig. 3B). Second, we focused on the
217 chromosome passenger complex (CPC: Bir1/Survivin, Sli15/INCENP, Nbl1/Borealin and
218 Ipl1/Aurora B), a complex known to regulate kinetochore-MT attachment dynamics (Cairo and
219 Lacefield, 2020). We found that inactivation of *IPL1* upon entry into quiescence using the
220 thermosensitive allele *ipl1-1* prevented Q-nMT bundle formation (Sup. Fig. 3C). The absence
221 of Q-nMT bundles in cells harboring the NA-PP1 kinase sensitive allele *ipl1-5as* (Nerusheva et
222 al., 2014) indicated that the Ipl1 kinase activity was required for this process (Fig. 3B and Sup.
223 Fig. 3D-E for controls). While we could not detect Ipl1 and Nbl1 in quiescent cells, we found

224 that Sli15-GFP and Bir1-GFP localized along the Q-nMT bundle with an enrichment at the Q-
225 nMT bundle +end (Fig. 3C). In 4-day-old *bir1Δ* cells, Q-nMT bundle were shorter and not fully
226 stabilized (Fig. 3D). In addition, inactivation of *SLI15* upon glucose exhaustion using the
227 thermosensitive allele *sli15-3* (Kim et al., 1999) drastically impaired Q-nMT bundle formation
228 (Sup. Fig. 3F). Finally, we examined the involvement of Bim1. Bim1 is a MT +end binding
229 protein that plays a role in kinetochore MT-end on attachment (Dudziak et al., 2021; Thomas
230 et al., 2016) and localizes along the entire Q-nMT bundle (Laporte et al., 2013). In fact, we
231 found that that the amount of Bim1 correlated with tubulin incorporation during Q-nMT
232 bundle formation (Sup. Fig. 3G). *BIM1* deletion alone has no effect on Q-nMT bundle
233 formation even in the presence of Noc ((Laporte et al., 2013) and Fig. 3D). However, *bim1Δ*
234 *bir1Δ* cells barely assembled MT structures, and these structures were sensitive to Noc (Fig.
235 3D). This demonstrates that in the absence of Bim1, Bir1 is critical for Q-nMT bundle
236 stabilization in phase I. Of note, we found that the viability of *bim1Δ bir1Δ* cells in quiescence
237 was drastically reduced (Sup Fig. 3H). Together, these experiments show that kinetochore-MT
238 attachments are critical for the initiation of Q-nMT bundle formation upon entry into
239 quiescence.

240 We then hypothesized that inter-kinetochore interactions could stabilize parallel MTs
241 embedded in the Q-nMT bundle. To test this idea, we analyzed MT organization in s*lk19Δ* cells
242 which are defective in kinetochore clustering (Richmond et al., 2013). In quiescence, Slk19-
243 GFP was enriched at both ends of the Q-nMT bundles (Fig. 3E). s*lk19Δ* cells displayed shorter
244 and thinner MT structures that were sensitive to Noc (Fig. 3F). Since Bim1 has been implicated
245 in kinetochore-kinetochore interaction, we combined s*lk19Δ* with *bim1Δ.* MT structures
246 detected in s*lk19Δ bim1Δ* cells barely reached ≈1 µm and disappeared upon Noc treatment.
247 In addition, in s*lk19Δ bim1Δ* cells, kinetochores localized as a rosette around the SPB (Fig. 3F)

248 and in s*lk19Δ bim1Δ* cell viability was severely impaired (Sup. Fig. 3H). This demonstrates that
249 in the absence of Bim1, Slk19 is required for MT bundling and stabilization in phase I. We then
250 focused on monopolin (Mam1, Lrs4, Hrr25 and Csm1), a complex that is known to cross-link
251 kinetochores (Corbett et al., 2010)). These proteins were found to be expressed in quiescent
252 cells (Sup. Fig. 3I) and when we analyzed the phenotype of *mam1Δ, lrs4Δ* and *csm1Δ* cells in
253 quiescence, most of them displayed short MT structures often arranged in a star-like array
254 (Fig. 3G-H and Sup. Fig. 3J). As for *bir1Δ* and *slk19Δ*, the combination of *bim1Δ* with monopolin
255 deletion worsened MT structure length and stability (Fig. 3H) as well as cell viability in
256 quiescence (Sup. Fig. 3H). Furthermore, cells deleted for *SPO13*, a gene encoding a protein
257 involved in monopolin recruitment to kinetochores (Lee et al., 2004) showed similar
258 phenotypes (Fig. 3G-H and Sup. Fig. 3H). Collectively, these experiments demonstrate that
259 inter-kinetochore interactions are critical for Q-nMT bundle assembly.

260 Finally, we investigated whether kinetochore-MT interactions were required for the
261 stability of Q-nMT bundle once it is formed. In 5-day-old WT cells, we used a UV-pulsed-laser
262 to break the Q-nMT bundle into two pieces. In most cases, the length of both the released
263 fragment and the fragment attached to the SPB remained constant, with the presence of
264 dynamic cMTs after laser pulse testifying for cell viability (Fig. 3I, Sup. Fig. 3K). In contrast, as
265 expected from previous studies (Khodjakov et al., 2004; Zareiesfandabadi and Elting, 2022), in
266 proliferating cells, dynamic anaphase spindles promptly disassembled after the laser-induced
267 breakage (Sup. Fig. 3L). This indicates that once Q-nMT bundles are formed, they do not
268 require MT-kinetochore interaction to be maintained. Accordingly, inactivation of Ndc80 (Sup.
269 Fig. 3B) or Ipl1 (Sup. Fig. 3M) in cells that were already in quiescence had no effect on the Q-
270 nMT bundle maintenance. Thus, once formed, Q-nMT stability is established and maintained
271 throughout its length.

272

273 **Each phase of Q-nMT bundle formation requires specific kinesins**

274 To further dissect the molecular mechanism of Q-nMT bundle formation, we focused
275 on kinesins. Kar3 is a kinesin that, in complex with its regulator Cik1, can generate parallel MT
276 bundles from a MT organizing center (MTOC) both *in vitro* and in proliferative cells (Manning
277 et al., 1999; Mieck et al., 2015; Molodtsov et al., 2016). In quiescence, we found that Kar3-
278 3GFP localized to the SPB, but also as dots along the Q-nMT bundle (Fig. 4A). In 4-day-old
279 *kar3Δ* cells, the majority of the detected MT structures were extremely short compared to WT
280 (Fig. 4B and for control without Noc see Sup Fig. 4A). Similar results were obtained in *cik1Δ*
281 but not in *vik1Δ* cells, which lack the alternative Kar3 regulators (Fig. 4B). Thus, the Kar3/Cik1
282 complex is required for phase I.

283 Cin8 is a kinesin-5 that cross-links MTs (Bodrug et al., 2020; Pandey et al., 2021; Singh
284 et al., 2018), and as such, could play a role in stabilizing Q-nMT bundles. Cin8 was barely
285 detectable in quiescent cells (Sup. Fig. 4B) and *cin8Δ* cells assembled Q-nMT bundles that were
286 thinner than in WT cells (Fig. 4C-E). However, these thinner bundles were stabilized in phase
287 III (Fig. 4C and Sup. Fig. 4C-D). Taken together, these results strongly suggest that Cin8 is
288 required for MT nucleation and/or elongation in phase II but not for MT bundle stabilization
289 in phase III.

290 Yeast have an additional kinesin-5 called Kip1 (Fridman et al., 2013). In quiescence,
291 most of the Kip1-GFP signal was observed at the Q-nMT bundle +end (Fig. 4F). In *kip1Δ* cells,
292 phase I was slightly delayed. In phase III, while as thick as WT Q-nMT bundles, MT bundles
293 detected in *kip1Δ* cells were not fully stabilized (Fig. 4G-H and Sup. Fig. 4E). These data
294 demonstrate that Kip1 is required for Q-nMT bundle stabilization in phase III. Of note, in phase
295 I and II, Q-nMT bundles were slightly longer in cells deleted for the kinesin-8 Kip3, a MT

296 depolymerase ((Fukuda et al., 2014), see Fig. 4H) but have a WT morphology in cells deleted
297 for Kip2, a kinesin that stabilizes cytoplasmic MTs ((Hibbel et al., 2015) and Sup. Fig. 4F). Taken
298 together, our results demonstrate that each phase of Q-nMT bundle assembly involves
299 specific kinesins.
300
301 **SPB duplication/separation requires Q-nMT bundle disassembly**
302 Finally, we questioned the molecular mechanism of Q-nMT bundle disassembly upon
303 exit from quiescence. We first found that cycloheximide prevented Q-nMT bundle disassembly
304 indicating that this process requires *de novo* protein synthesis (Fig. 5A). Then, we measured
305 Q-nMT bundle thickness upon depolymerization, and found that while Q-nMT bundles
306 shortened, they did not become thinner (Fig. 5B). In agreement, Nuf2-GFP clusters found at
307 the Q-nMT bundle +end moved back to the SPB while the Nuf2-GFP clusters localized along
308 the Q-nMT bundle remained immobile until they are reached by the +end-associated clusters
309 (Sup. Fig. 5A). This shows that not all MT +ends started depolymerizing at the same time, and
310 that longer MTs depolymerized first. This finding is consistent with our model in which MTs
311 are cross-linked along the entire length of the Q-nMT bundle.
312 Since Kip3 is the only well-characterized yeast MT depolymerase, we examined Q-nMT
313 bundle disassembly in *kip3Δ* cells and found that it was drastically delayed (Fig. 5C-D and Sup.
314 Fig. 5B), yet the overall depolymerization rate remained unaffected (Sup. Fig. 5B, left panel).
315 In fact, we found that in WT cells, Kip3 needed to be resynthesized upon exit from quiescence
316 (Sup. Fig. 5C). We searched for proteins that might be involved in Q-nMT bundle disassembly
317 together with Kip3. Among proteins required for mitotic spindle disassembly, we found that
318 inactivation of *CDC14*, *CDC15*, *CDH1*, *DCC1* and *TOR1* had no effect on Q-nMT bundle
319 disassembly, as did the inactivation of Ipl1 or proteins involved in kinetochore-MT attachment

320 (Sup. Fig. 5D-G). The only additional actor we found was She1, a dynein regulator (Bergman et
321 al., 2012), whose deletion strongly exacerbated the *kip3Δ* phenotype (Fig. 5C and Sup. Fig.
322 5H). Thus, Q-nMT bundle disassembly does not rely on the canonical mitotic spindle
323 disassembly machinery, but rather, specifically requires Kip3 and She1.

324 Importantly, when we followed quiescence exit at the single cell level,
325 depolymerization of the Q-nMT bundle always preceded SPB duplication/separation (Fig. 5A)
326 in both WT and in *kip3Δ* cells (Sup. Fig. 5B right panel). When we severely impeded Q-nMT
327 bundle disassembly using *kip3Δ she1Δ*, we found that SPB separation was greatly delayed (Fig.
328 5E-F, Sup. Fig. 5I-K). Besides, the proliferation rate of *kip3Δ she1Δ* cells was the same as WT
329 cells (Sup. Fig. 5I), and, upon quiescence exit, these mutant cells disassembled actin bodies as
330 fast as WT cells (Sup. Fig. 5K), demonstrating that *kip3Δ she1Δ* cells were not impaired in
331 sensing quiescence exit signals. These observations suggest that upon exit from quiescence,
332 the Q-nMT bundle has to be disassembled prior to SPB duplication/separation.

333 **Discussion**

334 Our results shed light on the precise temporal sequences that generate a Q-nMT
335 bundle upon quiescence establishment in yeast. From bacteria to human stem cells, changes
336 in cell physicochemical properties are known to accompany the establishment of quiescence.
337 Among these modifications, cellular volume reduction increases molecular crowding (Joyner
338 et al., 2016) and pH acidification both increases viscosity and causes changes in
339 macromolecule surface charges (Charruyer and Ghadially, 2018; Jacquel et al., 2021; Munder
340 et al., 2016; Persson et al., 2020). Much evidence suggests that these modifications act as
341 triggers for the auto-assembly of several types of enzyme-containing granules (Munder et al.,
342 2016; Petrovska et al., 2014; Rabouille and Alberti, 2017), or complex structures such as P-
343 bodies and Proteasome Storage Granules (Peters et al., 2013; Jacquel et al., 2021; Currie et
344 al., 2023). Recently, Molines and colleagues demonstrated that cytoplasmic viscosity
345 modulates MT dynamics *in vivo* (Molines et al., 2022). Here, we showed that the formation of
346 the Q-nMT bundle does not depend on changes in the physicochemical properties that cells
347 experience at the onset of quiescence establishment (Sup. Fig. 1). In fact, dynamic cMTs and
348 a stable Q-nMT bundle can be observed simultaneously in a quiescent cell (Sup. Fig. 1I), while
349 physicochemical properties evolve in parallel in both the nucleus and the cytoplasm (Joyner
350 et al., 2016). Importantly, cellular volume reduction, pH acidification and increased viscosity
351 are observed within minutes upon glucose starvation (Joyner et al., 2016) whereas the Q-nMT
352 bundles require a couple of days to be fully assembled (Fig. 1). Furthermore, Q-nMT bundle
353 formation cannot be delayed in time (Fig. 1H), and thus likely depends on a transient signal
354 emitted upon glucose depletion. We speculate that the SPB may act as a platform that
355 integrates this signal, and transfers it to the MT machinery in order to assemble a stable MT
356 structure.

357 As it is required for the onset of Q-nMT bundle formation (Fig. 3B), the CPC component
358 Aurora B/Ilp1, a kinase that plays a key role at the MT-kinetochore interface in response to
359 the tension status, could be one of the targets of the aforementioned nutritional signal. In
360 parallel, upon quiescence establishment, chromosome hyper-condensation (Guidi et al., 2015;
361 Rutledge et al., 2015) could modify the tension at the kinetochore/MT interface and as such
362 could contribute to the initiation of phase I (Fig. 6b). Besides, Bim1 has also been implicated
363 in MT-kinetochore attachment (Dudziak et al., 2021; Akhmanova and Steinmetz, 2015).
364 Although its deletion alone has no effect on Q-nMT bundle formation, its role becomes critical
365 for phase I when kinetochore-MT interactions are already destabilized by the absence of other
366 CPC components, other than Ipl1, such as Bir1 (Fig. 3D). Taken together, these observations
367 suggest that kinetochore-MT interactions are essential for phase I initiation, as confirmed by
368 the absence of Q-nMT bundle in the *ndc80-1* mutant (Fig. 3A).

369 In phase I, SPB-anchored MTs elongate and are concomitantly stabilized (Fig. 1A-C).
370 This step requires the kinesin-14 Kar3 and its regulator Cik1 (Fig. 4B). During mating
371 (Molodtsov et al., 2016), and in early mitosis, when half-spindles form (Kornakov et al., 2020),
372 Kar3/Cik1, together with Bim1, align and cross-link growing MTs along existing MTs, thereby
373 promoting the organization of MTs into parallel bundles. In mitosis however, the kinesin-
374 14/EB1 complex promotes MT dynamics (Kornakov et al., 2020). It remains to be determined
375 whether the robust MT stabilization in phase I, depends on the modification of the kinesin-
376 14/EB1 complex properties and/or on additional specific MT cross-linker(s) (Fig. 6c).

377 In quiescence, deletion of either monopolin or *SLK19* results in the formation of short,
378 shattered and flared MT structures, phenotypes that are exacerbated by the deletion of *BIM1*
379 (Fig. 3F-H). Since monopolin and Slk19 are involved in kinetochore clustering (Plowman et al.,
380 2019; Rabitsch et al., 2003; Tóth et al., 2000; Lee et al., 2004; Mittal et al., 2019; Movshovich

381 et al., 2008; Richmond et al., 2013; Zeng et al., 1999), we speculate that kinetochore-
382 kinetochore interaction may not only help prevent depolymerization of individual MTs, but
383 also constrain elongating phase I-MTs and facilitate their concomitant cross-linking (Fig. 6d).

384 With the initiation of phase I, Tub4 begins to accumulate at the SPB (Fig. 1E and Sup.
385 Fig. 1F) to enable the second wave of MT nucleation observed in phase II. As phase II-MTs
386 elongate, they are simultaneously stabilized along pre-existing phase I-MTs (Fig. 6d). This step
387 relies on the kinesin-5/Cin8 as Q-nMT bundles assembled in *cin8Δ* cells are thinner than WT
388 Q-nMT bundles (Fig. 4C-E). Intriguingly, *in vitro,* the monomeric form of the vertebrate kinesin-
389 5, Eg5, promotes MT nucleation and stabilizes lateral tubulin-tubulin contacts (Chen et al
390 2019). We assume that in the absence of Cin8, either nucleation of phase II-MTs cannot occur,
391 or phase II-MTs can elongate, but cannot be cross-linked and stabilized to pre-existing phase
392 I-MTs as they grow, and thus rapidly depolymerize. Absence of bundle thickening in phase II
393 is also observed in the "*Tub1-only*" mutant *i.e.* in the absence of Tub3 (Fig. 2D). Tubulin
394 isotypes or tubulin PTMs are known to promote the recruitment of specific kinesins and
395 thereby modify MT properties, see for example (Sirajuddin et al., 2014; Peris et al., 2009; Dunn
396 et al., 2008). Could Tub3 be important for Cin8 recruitment or function during phase II?

397 Following phase II, MTs elongate, but their distal parts (>1 µm) are not yet stable (Fig.
398 1A). Stabilization of full-length Q-nMT bundles is achieved approximately 4 days after glucose
399 exhaustion. This step depends on the kinesin-5/Kip1 (Fig. 4G-H and Sup. Fig. 4E) which is
400 essential for cross-linking and stabilizing elongating MTs during phase III (Fig. 6e). Accordingly,
401 we observed a Kip1 enrichment at the Q-nMT bundle +ends (Fig. 4F). Thus, consistent with
402 their ability to form homo-tetramers capable of cross-linking (Acar et al., 2013; Kapitein et al.,
403 2005; Scholey et al., 2014; Weinger et al., 2011) and stabilizing parallel MTs (Kapitein et al.,
404 2005; Shimamoto et al., 2015; Yukawa et al., 2020), and in addition to their role of sliding anti-

405 parallel MTs, the two yeast kinesin 5 are essential for Q-nMT bundle formation. However, in
406 quiescence, as well as in mitosis, Kip1 and Cin8 have non-equivalent functions (Roostalu et al.,
407 2011; Shapira and Gheber, 2016).

408 Thus far, our results indicate that the mechanism of Q-nMT bundle formation is distinct
409 from that of mitotic spindle assembly. Similarly, we show that Q-nMT bundle disassembly does
410 not involve the same pathway as mitotic spindle disassembly, as it requires Kip3 (Fig. 5C) but
411 is independent of the anaphase-promoting complex and Aurora B/Ipl1 (Sup. Fig. 5D-G).
412 Interestingly, the longest MTs begin to depolymerize from their +ends first. Then, when they
413 reach the +ends of shorter MTs, the shorter ones proceed to depolymerize alongside them
414 (Fig. 5B and Sup. Fig. 5A). This cooperative behavior has been observed *in vitro* within parallel
415 MT bundles (Laan et al., 2008). Our data demonstrate that such a comportment does exist *in*
416 *vivo*.

417 Finally, we show that the Q-nMT bundle is required for the survival of WT cells in
418 quiescence (Sup. Fig. 3H). While we do not yet know why this structure is important for
419 chronological aging, it is clear that the presence of the Q-nMT bundle modifies the
420 organization of the nucleus (Laporte et al., 2013; Laporte and Sagot, 2014; Laporte et al.,
421 2016). Since chromatin organization influences gene expression, one hypothesis could be that
422 the presence of the Q-nMT bundle is required for the expression of genes necessary for cell
423 survival in quiescence. Another attractive hypothesis is that the Q-nMT bundle could be the
424 yeast analog of the mammalian primary cilium. Indeed, these two structures are formed upon
425 proliferation cessation, they are both composed of highly stable parallel MTs, their formation
426 involves MT motors, and they are both templated from the centriole/SPB. More importantly,
427 we show here that Q-nMT bundle disassembly always occurs prior to SPB separation upon exit
428 from quiescence (Fig. 5E-F and Sup. Fig. 5J). Thus, the Q-nMT bundle disassembly may control

429 reentry into the proliferation cycle, just as the primary cilium does in ciliated mammalian cells

430 (Goto et al., 2017; Kim and Tsiokas, 2011).

431 ## Materiel and Methods

432 **Yeast strains, plasmids and growth conditions**

433 All the strains used in this study are isogenic to BY4741 (*mat a, leu2Δ0, his3Δ0, ura3Δ0,*
434 *met15Δ0)* or BY4742 (*mat alpha, leu2Δ0, his3Δ0, ura3Δ0, lys2Δ0),* available from GE
435 Healthcare Dharmacon Inc. (UK), except for Fig. 2, in which strains of the S288c background
436 were used (Nsamba et al., 2021) and Sup Fig 1F in which the W303 background was used. BY
437 strains carrying GFP fusions were obtained from ThermoFisher Scientific (Waltham, MA, USA).
438 Integrative plasmids p*Tub1-mTurquoise2-Tub1*, p*Tub1-wasabi-Tub1*, p*Tub1-mRUBY2-Tub1*,
439 p*Tub1-mEOS2-Tub1* were a generous gift from Wei-Lih Lee (Markus et al., 2015). The strain
440 expressing SPC42-mRFP1 is a generous gift from E. O'Shea (Huh et al., 2003). The strain
441 expressing TUB4-mTQZ is a generous gift from S. Jaspersen (Burns et al., 2015). The *ipl1-5as* is
442 a generous gift from A. Marston (Nerusheva et al, 2014). *Ipl1-1*, *ndc80-1* and *sli15-3* are
443 generous gift form C. Boone. Three copies of eGFP in tandem were integrated at the 3' end of
444 *DAD2*, *TUB3* or *KAR3* endogenous loci respectively. Plasmids for expressing Nup2-RFP (p3695)
445 or Bim1-3xGFP (p4587) from the endogenous locus were described in (Laporte et al., 2013).

446 For Fig. 1F and Sup. Fig. 1H, *pHIS3:mTurquoise2-Tub1+3'UTR::LEU2* was integrated at
447 *TUB1* locus, then a pRS303-*ADH2p-mRuby2-Tub1* was integrated at the *HIS3* locus. To
448 generate this plasmid, the *ADH2* promoter was amplified from yeast genomic DNA flanked
449 with NotI and SpeI restriction sites and inserted in pRS303. The mRuby2-Tub1+3'UTR,
450 including the 116-nucleotide intron and 618 nucleotides downstream the stop codon was
451 cloned between the SpeI and SalI sites.

452 Yeast cells were grown in liquid YPDA medium at 30 °C in flasks as described previously
453 in (Sagot et al., 2006) except for experiments using thermosensitive strains, where cells were
454 first grown at 25 °C then shifted at 37 °C for indicated time before imaging.

455 Experiment in Sup. Fig. 1J was performed as described in (Orij et al., 2009, Peters et al.,
456 2013). In brief, proliferating cells at an OD_{600nm} of 0.5 were transferred in Hepes buffer (25
457 mM Hepes, pH 7.4, 200 mM KCl, 1 mM $CaCl_2$, and 2 % dextrose), buffered either at pH 4 or
458 7.5, in the presence of 100 µM CCCP (Sigma-Aldrich). After 150 min at 30 °C with shaking, cells
459 were imaged (for mTQZ-Tub1) or fixed with formaldehyde and stained using Alexa Fluor 568–
460 phalloidin (Invitrogen) as described (Sagot et al., 2006).

461 For live cell imaging, 2 µL of the cell culture were spotted onto a glass slide and
462 immediately imaged at room temperature.

463 For quiescence exit (Fig. 5), cells were first incubated 2-3 min in liquid YPD and then 2
464 µL were spread onto a 2 % agarose microscope pad containing YPD. Individual cells were
465 imaged every hour, up to 6 or 12 h at 21°C. For quiescence exit in presence of cycloheximide
466 (Fig. 5A), cells were pre-incubated 30 min in the presence of the drug prior quiescence exit.

467 Immunofluorescence was done as in (Laporte et al. 2016), and AlexaFluor Phalloidin
468 (Invitrogen) staining as in (Sagot et al., 2006).

469 Cycloheximide was used at 180 µM (Sigma-Aldrich), Nocodazole was used at 30 µg/mL
470 (7.5 µM) (Sigma-Aldrich), NA-PP1 was used at 50 µM (Sigma-Aldrich).

471 **Fluorescence Microscopy**

472 Cells were observed on a fully-automated Zeiss 200M inverted microscope (Carl Zeiss,
473 Thornwood, NY, USA) equipped with an MS-2000 stage (Applied Scientific Instrumentation,
474 Eugene, OR, USA), a Lambda LS 300 W xenon light source (Sutter, Novato, CA, USA), a 100X
475 1.4NA Plan-Apochromat objective, and a 5-position filter turret. For RFP and mRuby2 imaging
476 we used a Cy3 filter (Ex: HQ535/50 nm – Em: HQ610/75 nm – BS: Q565 nm lp). For GFP
477 imaging, we used a FITC filter (excitation, HQ487/25 nm; emission, HQ535/40 nm; beam
478 splitter, Q505 nm lp). For mTurquoise2 imaging we used a DAPI filter (Ex: 360/40 nm – Em:

479 460/50 nm– BS: 400 nm). All the filters are from Chroma Technology Corp. Images were
480 acquired using a CoolSnap HQ camera (Roper Scientific, Tucson, AZ, USA). The microscope,
481 camera, and shutters (Uniblitz, Rochester, NY, USA) were controlled by SlideBook software 5.
482 0. (Intelligent Imaging Innovations, Denver, CO, USA).

483 For PALM (Fig. 4E) a Nikon Ti-Eclipse equipped with iLas2 TIRF arm, laser diodes (405,
484 488, 532, 561, 642 nm), a 100x 1.49 oil (TIRF) objective connected to a EMCCD Camera
485 Photometrics Evolve was used.

486 For expansion microscopy (Sup Fig. 2A and 3A), spheroplasts were obtained as
487 described in (Laporte et al., 2016). After washing in 10 mg/mL NaBH4 in PEMS for 10 min,
488 spheroplasts were seeded on 12 mm round poly-L-lysine coated coverslips, washed twice for
489 30 min in 100 µL PEM-BAL (PEM + 1 % BSA) and incubated with the primary antibodies (anti-
490 GFP from mouse; Roche, ref. 11814460001, 1/50; anti-alpha-tubulin from rat; YOL1/34,
491 Abcam, ref. Ab6161, 1/100) for 1 hour at 37 °C. Cells were then washed three times in PEM-
492 BAL and incubated with the secondary antibodies (Goat anti-mouse AlexaFluor®488 1/200 and
493 Donkey anti-rat AlexaFluor®555; A11029 and A21434 respectively, ThermoFisher Scientific,
494 Waltham, MA) for 45 min at 37 °C. Cells were then washed three times with PBS. Cells were
495 processed for Expansion Microscopy as previously described in (Bahri et al., 2021).
496 Spheroplasts were incubated for 10 min in 0.25 % GA in PBS, washed in PBS three times for 5
497 min, and processed for gelation. A drop of 100 µL of ExM MS (8.625 % (wt/wt) SA, 2.5 %
498 (wt/wt) AA, 0.15 % (wt/wt) BIS, 2 M NaCl in 1× PBS) was placed on the chilled Parafilm, and
499 coverslips were put on the drop with cells facing the solution and incubated for 3 min. Then
500 the coverslips were transferred to 35 µL of ExM MS supplemented with 0.2 % APS and 0.2 %
501 TEMED, with the initiator (APS) added last. Gelation proceeded for 3 min on ice, and samples
502 were incubated at 37 °C in a humidified chamber in the dark for 1 h. Then coverslips with

503 attached gels were transferred into a six-well plate for incubation in 2 mL of digestion buffer
504 (1× TAE buffer, 0.5 % Triton X-100, 0.8 M guanidine hydrochloride, pH ~8.3) supplemented
505 with DAPI (1 µg/mL) for 10-15 min at 37 °C, until the gels detached. Fresh proteinase K at 8
506 units/mL was then added and samples incubated at 37 °C for 30 min. Finally, gels were
507 removed and placed in 10 mL petri dishes filled with ddH2O for expansion. Water was
508 exchanged at least twice every 30 min, and incubated in ddH2O overnight at RT. Gels
509 expanded between 4× and 4.2× according to SA purity. Expanded cells were imaged with a
510 UPlanS Apo 100X/1.4 oil immersion objective in an Olympus IX81 microscope (Olympus,
511 Tokyo, Japan). For structured illumination microscopy (Sup Fig 3A), a ZEISS Elyra 7 Lattice SIM
512 was used.

513 Laser ablation (Fig. 3I and Sup. Fig. 3K-L) was performed at room temperature with a
514 100X oil Plan-Apochromat objective lens (NA 1.4) and an Axio-Observed.Z1 microscope (Carl
515 Zeiss) equipped with a spinning disk confocal (Yokogawa), an EMCCD Evolve camera
516 (Photometrics and Roper Scientific) and 491 nm (100 mW; Cobolt calypso) and 561 nm (100
517 mW; Cobolt Jive) lasers. Images were acquired with Metamorph software (Roper Scientific).
518 Every 30 to 120 s, a Z-series of 0.4 µm steps were acquired. A 355 nm microchip laser (Teem
519 Photonics) with a 21 kHz repetition rate, 0.8 µJ energy/pulse, 2 kW of peak power and 400 ps
520 pulse width, powered with an iLas2 PULSE system (Roper Scientific) was used between 10 to
521 40 % power with one pulse of a spot length of 100 points. Breakage was considered as
522 successful if a non-alignment between the two remaining Q-n MT bundle fragments was
523 observed.

524 Z-stacks were deconvolved using the Deconvolution Lab plugin (Fig. 1D, F; Fig. 3C, E, F;
525 Fig. 4A, F; Sup. Fig. 1E; Sup. Fig. 2A and Sup. Fig. 4B).

526 In Fig. 1H, F, Fig. 2B-C, Fig. 3C, Fig. 4D, G, Sup. Fig. 1I, Sup. Fig. 2E and Sup. Fig. 3A, a
527 fuzzy fluorescence signal was detected in some cell cytoplasm using the GFP long pass filter
528 set. This signal is not GFP but rather due to a non-specific yellow background fluorescence.

529 **Image analysis**

530 Distribution and associated statistics were performed using GraphPad Prism 5
531 (GraphPad Software, Inc. La Jolla, USA) and Excel (Microsoft). Unless specified, a student test
532 (t-test with two independent samples) was used to compare two conditions. Among p-values
533 obtained for biological repetitions of the same experiment (Fig. 1A; Fig. 2B-C, Fig. 3A, D, F, H;
534 Fig. 4C, H, and Fig. 5C), the indicated p-values are the highest calculated among the repeated
535 experiments. p-values above 0,05 are indicated, while p-values below 0,05 are indicated using
536 ** (0,05 > p-value > $1\ 10^{-4}$) and *** if the p-values was less than $1\ 10^{-5}$). In histograms and
537 scatter dot plots, the mean is shown and the error bars indicate SD.

538 MT length was measured on MAX-projected image using imageJ.

539 For MT fluorescence intensity measurements (Fig. 1B, Fig. 2D, Fig. 4D, Sup. Fig. 1A, and
540 Sup. Fig. 4C, E), a line scan (i1) of 4 pixels width containing both FP signal and background was
541 drawn along MTs on sum projection image (3-4 Z-plans) using ImageJ. A line of 8 pixels width
542 (at the same location) was drawn in order to calculate the intensity of the surrounding
543 background (i2). The real intensity (ir) was calculated as follow ir = [i1 - ([(i2 x $i2_{surface}$) - (i1 x
544 $i1_{surface}$)] / ($i2_{surface}$ - $i1_{surface}$)) * $i1_{surface}$]. We arbitrarily set the 'zero' at 0,5µm before the
545 fluorescence increased onset on the SPB side in order to align all intensity measurements.
546 Similarly, to measure Tub4 fluorescence intensity (Fig. 1E and Sup. Fig. 1F). two boxes (i1) and
547 (i2) were drawn around the fluorescence signal. Intensity was calculated as follow: int = [i1 -
548 ([(i2 x $i2_{surface}$) - (i1 x $i1_{surface}$)] / ($i2_{surface}$ - $i1_{surface}$)) * $i1_{surface}$].

549 For morphometric Q-nMT bundle property distribution (Fig. 1C, Fig. 4B and Sup. Fig.
550 4A, D) the mean fluorescence intensity was measured in each individual cell, in a finite area
551 localized adjacent to the SPB (0,4 µm – 3-4 Z stack sum projected) as an estimate of Q-nMT
552 bundle width, and plotted as a function of the corresponding bundle length.

553 For Nuf2-GFP fluorescence intensity measurement at the SPB (Sup. Fig. 1E, bottom
554 panel), GFP and RFP line scan measurements were done on a 4 Z-planes sum projection. The
555 "SPB localization zone" was defined as the length ending 250 µm after the brightest RFP signal
556 of Spc42-RFP. The remaining Q-nMT bundle zone was defined as the "+end zone". The total
557 Nuf2-GFP signal detected along the Q-nMT bundle was set to 100 % to determine the
558 percentage of the signal measured at the "SPB localization zone" and the "+end zone".

559 Normalized Q-nMT bundle length (Fig. 3C, and Fig. 4A, F) was calculated after line scan
560 intensity measurement. mTQZ-Tub1 intensity slopes were first aligned on their inflexion
561 points. To compare Q-nMT bundles with different lengths, we first sorted Q-nMT bundles <
562 1.8 µm. After an artificial isotropic expansion, we fit all MT structures to the same length.
563 Then, the corresponding mean intensity of Q-nMT bundles (mTZQ-Tub1) and GFP signal were
564 calculated.

565 To measure Q-nMT bundle depolymerization rate (Fig. 5A and Sup. Fig. 5B), individual
566 Q-nMT bundle lengths were measured over time. The first length measurement was set to
567 100 %. A fluorescence drop above or equal to 25 % defines the inflexion point of the slope,
568 and was used to align the length measurements for Q-nMT bundles.

569 The FWHM (Full Width at Half Maximum, Fig. 5B and Sup. Fig. 1B) was calculated by
570 measuring fluorescence intensity of a line crossing perpendicularly a Q-nMT bundle, at 0.5 µm
571 from the SPB, using a sum projection image. After fitting the intensity level with Gaussian

572 distribution and obtaining the standard deviation (σ) value, FWHM was calculated using the
573 equation $2\sqrt{(2\ln 2)}\times\sigma$.

574 **Western blots**

575 Western blots were done as described in (Sagot et al., 2006) using anti-GFP antibodies
576 (Abcam); anti-Tat1 antibodies (a generous gift from J-P. Javerzat) and antibody against the
577 budding yeast Act1 or Sac6, generous gifts from B. Goode and anti-TagRFP (mRuby2)
578 antibodies, a generous gift from M. Rojo.

579 **Phenotypical analysis of cells without Q-nMT bundle**

580 WT cells were grown to glucose exhaustion (OD ~6.5) (Fig. 1F) or for 5 d (Sup. Fig. 1L),
581 washed with "old YPDA" (YPDA medium in which cells were grown for 4 d and then filtered to
582 remove cells) and treated with either DMSO or Noc (30µg/mL) for 24 h. Cells were then
583 washed twice in "old YPDA" before being incubated in the same medium. Dead cells were
584 identified using methylene blue staining. The capacity of cells to exit quiescence (Sup. Fig. 1L,
585 right panel) was scored after micro-manipulation of live cells (cells not stained with methylene
586 blue) as described in (Laporte et al., 2011) (N=4, n>100).

587

588 ## Supplemental data

589 **Supplementary Figure 1** further describes the 3 steps of Q-nMT bundle formation. It shows
590 the impact of physicochemical cell properties on MT stabilization and demonstrates that Q-
591 nMT bundle is required for both cell viability in quiescence and quiescence exit fitness.

592 **Supplementary Figure 2** describes the impact of the alpha tubulin level on Q-nMT bundle
593 assembly.

594 **Supplementary Figure 3** demonstrates that kinetochore-MT interactions are not required for
595 Q-nMT bundle maintenance and that mutants affected for kinetochore-kinetochore
596 interactions have reduced viability in quiescence.

597 **Supplementary Figure 4** further describes the impact of kinesin deletion on Q-nMT bundle
598 morphometric parameters.

599 **Supplementary Figure 5** explores Q-nMT bundle disassembly in mutants involved in mitotic
600 spindle dismantlement.

601

Acknowledgments

The authors would like to thank the Bordeaux Imaging center for the help in super-resolution imaging. We express our gratitude to E. O'Shea, A. Marston, S. Jaspersen, J-P. Javerzat, Wei-Lih Lee, C. Boone and B. Goode for sharing reagents and M. Rojo for providing us with the mCherry specific antibodies. We thank Michaël Gué (Zeiss) for helping us a with the lattice SIM Elyra 7 microscope. We would like to thank J-P. Javerzat for helpful and constructive discussions about our work. DL, AML, JD and IS were supported by a grant from the ANR-21-CE13-0023-01, la Ligue Contre le Cancer Régionale – Dordogne grant #193366 and the CNRS. MG and EN were supported by a National Science Foundation grant number MCB-1846262. AR was supported by the Conseil Régional de Nouvelle Aquitaine (#20111301010) and the CNRS.

Author Contributions

D. Laporte did all the experiments described in this manuscript, except Fig. 1F, 1H, Fig. 5E-F, Sup. Fig. 1H, Sup. Fig. 3E, J and Sup. Fig. 5I to K that were performed by A. Massoni-Laporte, together with all image deconvolution, and Fig. 4E and Sup. Fig. 2A and 3A that were done by J. Dompierre. A. Royou helped for pulse-laser experiments of Fig. 3I and Sup Fig. 3K and L. C. Lefranc did molecular biology and western blots. D. Mauboules performed yeast genetic for Fig. 2. M. L. Gupta Jr and E. T. Nsamba created the Tub1-only mutant (Fig. 2). L. Gal and M. Schuldiner performed high throughput deletion screen. IS and DL designed and supervised the experiments. IS and DL wrote the manuscript.

624 **References**

625 Acar, S., D.B. Carlson, M.S. Budamagunta, V. Yarov-Yarovoy, J.J. Correia, M.R. Niñonuevo, W. Jia, L.
626 Tao, J.A. Leary, J.C. Voss, J.E. Evans, and J.M. Scholey. 2013. The bipolar assembly domain of
627 the mitotic motor kinesin-5. Nat Commun. 4:1343. doi:10.1038/ncomms2348.

628 Aiken, J., J.K. Moore, and E.A. Bates. 2019. TUBA1A mutations identified in lissencephaly patients
629 dominantly disrupt neuronal migration and impair dynein activity. Human Molecular
630 Genetics. 28:1227–1243. doi:10.1093/hmg/ddy416.

631 Akhmanova, A., and M.O. Steinmetz. 2015. Control of microtubule organization and dynamics: two
632 ends in the limelight. Nature Reviews Molecular Cell Biology. 16:711–726.
633 doi:10.1038/nrm4084.

634 Anvarian, Z., K. Mykytyn, S. Mukhopadhyay, L.B. Pedersen, and S.T. Christensen. 2019. Cellular
635 signalling by primary cilia in development, organ function and disease. Nat Rev Nephrol.
636 15:199–219. doi:10.1038/s41581-019-0116-9.

637 Baas, P.W., A.N. Rao, A.J. Matamoros, and L. Leo. 2016. Stability properties of neuronal microtubules.
638 Cytoskeleton (Hoboken). 73:442–460. doi:10.1002/cm.21286.

639 Bahri, H., J. Buratto, M. Rojo, J.P. Dompierre, B. Salin, C. Blancard, S. Cuvellier, M. Rose, A. Ben
640 Ammar Elgaaied, E. Tetaud, J.-P. di Rago, A. Devin, and S. Duvezin-Caubet. 2021. TMEM70
641 forms oligomeric scaffolds within mitochondrial cristae promoting in situ assembly of
642 mammalian ATP synthase proton channel. Biochim Biophys Acta Mol Cell Res. 1868:118942.
643 doi:10.1016/j.bbamcr.2020.118942.

644 Bergman, Z.J., X. Xia, I.A. Amaro, and T.C. Huffaker. 2012. Constitutive dynein activity in She1
645 mutants reveals differences in microtubule attachment at the yeast spindle pole body. Mol
646 Biol Cell. 23:2319–2326. doi:10.1091/mbc.E12-03-0223.

647 Bodakuntla, S., A.S. Jijumon, C. Villablanca, C. Gonzalez-Billault, and C. Janke. 2019. Microtubule-
648 Associated Proteins: Structuring the Cytoskeleton. Trends Cell Biol. 29:804–819.
649 doi:10.1016/j.tcb.2019.07.004.

650 Bode, C.J., M.L. Gupta, K.A. Suprenant, and R.H. Himes. 2003. The two alpha-tubulin isotypes in
651 budding yeast have opposing effects on microtubule dynamics in vitro. EMBO Rep. 4:94–99.
652 doi:10.1038/sj.embor.embor716.

653 Bodrug, T., E.M. Wilson-Kubalek, S. Nithianantham, A.F. Thompson, A. Alfieri, I. Gaska, J. Major, G.
654 Debs, S. Inagaki, P. Gutierrez, L. Gheber, R.J. McKenney, C.V. Sindelar, R. Milligan, J. Stumpff,
655 S.S. Rosenfeld, S.T. Forth, and J. Al-Bassam. 2020. The kinesin-5 tail domain directly
656 modulates the mechanochemical cycle of the motor domain for anti-parallel microtubule
657 sliding. eLife. 9:e51131. doi:10.7554/eLife.51131.

658 Burns, S., J.S. Avena, J.R. Unruh, Z. Yu, S.E. Smith, B.D. Slaughter, M. Winey, and S.L. Jaspersen. 2015.
659 Structured illumination with particle averaging reveals novel roles for yeast centrosome
660 components during duplication. Elife. 4. doi:10.7554/eLife.08586.

661 Cairo, G., and S. Lacefield. 2020. Establishing correct kinetochore-microtubule attachments in mitosis
662 and meiosis. Essays in Biochemistry. 64:277–287. doi:10.1042/EBC20190072.

663 Charruyer, A., and R. Ghadially. 2018. Influence of pH on Skin Stem Cells and Their Differentiation.
664 Curr Probl Dermatol. 54:71–78. doi:10.1159/000489520.

665 Cheeseman, I.M., J.S. Chappie, E.M. Wilson-Kubalek, and A. Desai. 2006. The conserved KMN
666 network constitutes the core microtubule-binding site of the kinetochore. Cell. 127:983–997.
667 doi:10.1016/j.cell.2006.09.039.

668 Cleary, J.M., and W.O. Hancock. 2021. Molecular mechanisms underlying microtubule growth
669 dynamics. Curr Biol. 31:R560–R573. doi:10.1016/j.cub.2021.02.035.

670 Corbett, K.D., C.K. Yip, L.-S. Ee, T. Walz, A. Amon, and S.C. Harrison. 2010. The monopolin complex
671 crosslinks kinetochore components to regulate chromosome-microtubule attachments. Cell.
672 142:556–567. doi:10.1016/j.cell.2010.07.017.

673 Currie, S.L., W. Xing, D. Muhlrad, C.J. Decker, R. Parker, and M.K. Rosen. 2023. Quantitative
674 reconstitution of yeast RNA processing bodies. Proc Natl Acad Sci U S A. 120:e2214064120.
675 doi:10.1073/pnas.2214064120.

676 DeLuca, K.F., A. Meppelink, A.J. Broad, J.E. Mick, O.B. Peersen, S. Pektas, S.M.A. Lens, and J.G.
677 DeLuca. 2018. Aurora A kinase phosphorylates Hec1 to regulate metaphase kinetochore-
678 microtubule dynamics. J Cell Biol. 217:163–177. doi:10.1083/jcb.201707160.

679 Dudziak, A., L. Engelhard, C. Bourque, B.U. Klink, P. Rombaut, N. Kornakov, K. Jänen, F. Herzog, C.
680 Gatsogiannis, and S. Westermann. 2021. Phospho-regulated Bim1/EB1 interactions trigger
681 Dam1c ring assembly at the budding yeast outer kinetochore. EMBO J. 40:e108004.
682 doi:10.15252/embj.2021108004.

683 Dunn, S., E.E. Morrison, T.B. Liverpool, C. Molina-París, R.A. Cross, M.C. Alonso, and M. Peckham.
684 2008. Differential trafficking of Kif5c on tyrosinated and detyrosinated microtubules in live
685 cells. J Cell Sci. 121:1085–1095. doi:10.1242/jcs.026492.

686 Fridman, V., A. Gerson-Gurwitz, O. Shapira, N. Movshovich, S. Lakämper, C.F. Schmidt, and L. Gheber.
687 2013. Kinesin-5 Kip1 is a bi-directional motor that stabilizes microtubules and tracks their
688 plus-ends in vivo. J Cell Sci. 126:4147–4159. doi:10.1242/jcs.125153.

689 Fukuda, Y., A. Luchniak, E.R. Murphy, and M.L. Gupta. 2014. Spatial control of microtubule length and
690 lifetime by opposing stabilizing and destabilizing functions of Kinesin-8. Curr Biol. 24:1826–
691 1835. doi:10.1016/j.cub.2014.06.069.

692 Goodson, H.V., and E.M. Jonasson. 2018. Microtubules and Microtubule-Associated Proteins. Cold
693 Spring Harb Perspect Biol. 10:a022608. doi:10.1101/cshperspect.a022608.

694 Goto, H., H. Inaba, and M. Inagaki. 2017. Mechanisms of ciliogenesis suppression in dividing cells. Cell
695 Mol Life Sci. 74:881–890. doi:10.1007/s00018-016-2369-9.

696 Gudimchuk, N.B., and J.R. McIntosh. 2021. Regulation of microtubule dynamics, mechanics and
697 function through the growing tip. Nat Rev Mol Cell Biol. 22:777–795. doi:10.1038/s41580-
698 021-00399-x.

699 Guidi, M., M. Ruault, M. Marbouty, I. Loïodice, A. Cournac, C. Billaudeau, A. Hocher, J. Mozziconacci,
700 R. Koszul, and A. Taddei. 2015. Spatial reorganization of telomeres in long-lived quiescent
701 cells. Genome Biol. 16:206. doi:10.1186/s13059-015-0766-2.

Hahn, I., A. Voelzmann, Y.-T. Liew, B. Costa-Gomes, and A. Prokop. 2019. The model of local axon homeostasis - explaining the role and regulation of microtubule bundles in axon maintenance and pathology. Neural Dev. 14:11. doi:10.1186/s13064-019-0134-0.

Heald, R., and A. Khodjakov. 2015. Thirty years of search and capture: The complex simplicity of mitotic spindle assembly. J Cell Biol. 211:1103–1111. doi:10.1083/jcb.201510015.

Hibbel, A., A. Bogdanova, M. Mahamdeh, A. Jannasch, M. Storch, E. Schäffer, D. Liakopoulos, and J. Howard. 2015. Kinesin Kip2 enhances microtubule growth in vitro through length-dependent feedback on polymerization and catastrophe. Elife. 4:e10542. doi:10.7554/eLife.10542.

Huh, W.-K., J.V. Falvo, L.C. Gerke, A.S. Carroll, R.W. Howson, J.S. Weissman, and E.K. O'Shea. 2003. Global analysis of protein localization in budding yeast. Nature. 425:686–691. doi:10.1038/nature02026.

Jacquel, B., T. Aspert, D. Laporte, I. Sagot, and G. Charvin. 2021. Monitoring single-cell dynamics of entry into quiescence during an unperturbed life cycle. Elife. 10:e73186. doi:10.7554/eLife.73186.

Janke, C., and M.M. Magiera. 2020. The tubulin code and its role in controlling microtubule properties and functions. Nat Rev Mol Cell Biol. 21:307–326. doi:10.1038/s41580-020-0214-3.

Jin, Q., E. Trelles-Sticken, H. Scherthan, and J. Loidl. 1998. Yeast nuclei display prominent centromere clustering that is reduced in nondividing cells and in meiotic prophase. J. Cell Biol. 141:21–29.

Joyner, R.P., J.H. Tang, J. Helenius, E. Dultz, C. Brune, L.J. Holt, S. Huet, D.J. Müller, and K. Weis. 2016. A glucose-starvation response regulates the diffusion of macromolecules. Elife. 5. doi:10.7554/eLife.09376.

Kapitein, L.C., E.J.G. Peterman, B.H. Kwok, J.H. Kim, T.M. Kapoor, and C.F. Schmidt. 2005. The bipolar mitotic kinesin Eg5 moves on both microtubules that it crosslinks. Nature. 435:114–118. doi:10.1038/nature03503.

Khodjakov, A., S. La Terra, and F. Chang. 2004. Laser Microsurgery in Fission Yeast: Role of the Mitotic Spindle Midzone in Anaphase B. Current Biology. 14:1330–1340. doi:10.1016/j.cub.2004.07.028.

Kim, J.H., J.S. Kang, and C.S. Chan. 1999. Sli15 associates with the ipl1 protein kinase to promote proper chromosome segregation in Saccharomyces cerevisiae. *J. Cell Biol.* 145:1381–1394. doi:10.1083/jcb.145.7.1381.

Kim, S., and L. Tsiokas. 2011. Cilia and cell cycle re-entry: more than a coincidence. Cell Cycle. 10:2683–2690. doi:10.4161/cc.10.16.17009.

Kirschner, M., and T. Mitchison. 1986. Beyond self-assembly: from microtubules to morphogenesis. Cell. 45:329–342.

Khodjakov, A., S. La Terra, and F. Chang. 2004. Laser Microsurgery in Fission Yeast: Role of the Mitotic Spindle Midzone in Anaphase B. *Curr. Biol.* 14:1330–1340. doi:10.1016/j.cub.2004.07.028.

739 Kornakov, N., B. Möllers, and S. Westermann. 2020. The EB1-Kinesin-14 complex is required for
740 efficient metaphase spindle assembly and kinetochore bi-orientation. J Cell Biol. 219.
741 doi:10.1083/jcb.202003072.

742 Laan, L., J. Husson, E.L. Munteanu, J.W.J. Kerssemakers, and M. Dogterom. 2008. Force-generation
743 and dynamic instability of microtubule bundles. Proc Natl Acad Sci U S A. 105:8920–8925.
744 doi:10.1073/pnas.0710311105.

745 Laporte, D., F. Courtout, B. Pinson, J. Dompierre, B. Salin, L. Brocard, and I. Sagot. 2015. A stable
746 microtubule array drives fission yeast polarity reestablishment upon quiescence exit. J. Cell
747 Biol. 210:99–113. doi:10.1083/jcb.201502025.

748 Laporte, D., F. Courtout, B. Salin, J. Ceschin, and I. Sagot. 2013. An array of nuclear microtubules
749 reorganizes the budding yeast nucleus during quiescence. J. Cell Biol. 203:585–594.
750 doi:10.1083/jcb.201306075.

751 Laporte, D., F. Courtout, S. Tollis, and I. Sagot. 2016. Quiescent Saccharomyces cerevisiae forms
752 telomere hyperclusters at the nuclear membrane vicinity through a multifaceted mechanism
753 involving Esc1, the Sir complex, and chromatin condensation. Mol. Biol. Cell. 27:1875–1884.
754 doi:10.1091/mbc.E16-01-0069.

755 Laporte, D., and I. Sagot. 2014. Microtubules move the nucleus to quiescence. Nucleus. 5:113–118.
756 doi:10.4161/nucl.28538.

757 Lee, B.H., B.M. Kiburz, and A. Amon. 2004. Spo13 maintains centromeric cohesion and kinetochore
758 coorientation during meiosis I. Curr Biol. 14:2168–2182. doi:10.1016/j.cub.2004.12.033.

759 Liu, P., M. Würtz, E. Zupa, S. Pfeffer, and E. Schiebel. 2021. Microtubule nucleation: The waltz
760 between γ-tubulin ring complex and associated proteins. Curr Opin Cell Biol. 68:124–131.
761 doi:10.1016/j.ceb.2020.10.004.

762 Manning, B.D., J.G. Barrett, J.A. Wallace, H. Granok, and M. Snyder. 1999. Differential regulation of
763 the Kar3p kinesin-related protein by two associated proteins, Cik1p and Vik1p. J Cell Biol.
764 144:1219–1233. doi:10.1083/jcb.144.6.1219.

765 Markus, S.M., S. Omer, K. Baranowski, and W.-L. Lee. 2015. Improved Plasmids for Fluorescent
766 Protein Tagging of Microtubules in Saccharomyces cerevisiae. Traffic. 16:773–786.
767 doi:10.1111/tra.12276.

768 Meiring, J.C.M., B.I. Shneyer, and A. Akhmanova. 2020. Generation and regulation of microtubule
769 network asymmetry to drive cell polarity. Curr Opin Cell Biol. 62:86–95.
770 doi:10.1016/j.ceb.2019.10.004.

771 Mieck, C., M.I. Molodtsov, K. Drzewicka, B. van der Vaart, G. Litos, G. Schmauss, A. Vaziri, and S.
772 Westermann. 2015. Non-catalytic motor domains enable processive movement and
773 functional diversification of the kinesin-14 Kar3. eLife. 4:e04489. doi:10.7554/eLife.04489.

774 Mitchison, T., and M. Kirschner. 1984. Dynamic instability of microtubule growth. Nature. 312:237–
775 242.

776 Mittal, P., A. Chavan, D. Trakroo, S. Shah, and S.K. Ghosh. 2019. Outer kinetochore protein Dam1
777 promotes centromere clustering in parallel with Slk19 in budding yeast. Chromosoma.
778 128:133–148. doi:10.1007/s00412-019-00694-9.

779 Molines, A.T., J. Lemière, M. Gazzola, I.E. Steinmark, C.H. Edrington, C.-T. Hsu, P. Real-Calderon, K.
780 Suhling, G. Goshima, L.J. Holt, M. Thery, G.J. Brouhard, and F. Chang. 2022. Physical
781 properties of the cytoplasm modulate the rates of microtubule polymerization and
782 depolymerization. Developmental Cell. 57:466-479.e6. doi:10.1016/j.devcel.2022.02.001.

783 Molodtsov, M.I., C. Mieck, J. Dobbelaere, A. Dammermann, S. Westermann, and A. Vaziri. 2016. A
784 Force-Induced Directional Switch of a Molecular Motor Enables Parallel Microtubule Bundle
785 Formation. Cell. 167:539-552.e14. doi:10.1016/j.cell.2016.09.029.

786 Movshovich, N., V. Fridman, A. Gerson-Gurwitz, I. Shumacher, I. Gertsberg, A. Fich, M.A. Hoyt, B.
787 Katz, and L. Gheber. 2008. Slk19-dependent mid-anaphase pause in kinesin-5-mutated cells. J
788 Cell Sci. 121:2529–2539. doi:10.1242/jcs.022996.

789 Munder, M.C., D. Midtvedt, T. Franzmann, E. Nüske, O. Otto, M. Herbig, E. Ulbricht, P. Müller, A.
790 Taubenberger, S. Maharana, L. Malinovska, D. Richter, J. Guck, V. Zaburdaev, and S. Alberti.
791 2016. A pH-driven transition of the cytoplasm from a fluid- to a solid-like state promotes
792 entry into dormancy. eLife. 5:e09347. doi:10.7554/eLife.09347.

793 Muroyama, A., and T. Lechler. 2017. Microtubule organization, dynamics and functions in
794 differentiated cells. Development. 144:3012–3021. doi:10.1242/dev.153171.

795 Nerusheva, O.O., S. Galander, J. Fernius, D. Kelly, and A.L. Marston. 2014. Tension-dependent
796 removal of pericentromeric shugoshin is an indicator of sister chromosome biorientation.
797 *Genes Dev.* 28:1291–1309. doi:10.1101/gad.240291.114.

798 Nsamba, E.T., A. Bera, M. Costanzo, C. Boone, and M.L. Gupta Jr. 2021. Tubulin isotypes optimize
799 distinct spindle positioning mechanisms during yeast mitosis. Journal of Cell Biology.
800 220:e202010155. doi:10.1083/jcb.202010155.

801 Orij, R., J. Postmus, A. Ter Beek, S. Brul, and G.J. Smits. 2009. In vivo measurement of cytosolic and
802 mitochondrial pH using a pH-sensitive GFP derivative in Saccharomyces cerevisiae reveals a
803 relation between intracellular pH and growth. Microbiology. 155:268–278.
804 doi:https://doi.org/10.1099/mic.0.022038-0.

805 Pandey, H., M. Popov, A. Goldstein-Levitin, and L. Gheber. 2021. Mechanisms by Which Kinesin-5
806 Motors Perform Their Multiple Intracellular Functions. Int J Mol Sci. 22:6420.
807 doi:10.3390/ijms22126420.

808 Peris, L., M. Wagenbach, L. Lafanechère, J. Brocard, A.T. Moore, F. Kozielski, D. Job, L. Wordeman,
809 and A. Andrieux. 2009. Motor-dependent microtubule disassembly driven by tubulin
810 tyrosination. J Cell Biol. 185:1159–1166. doi:10.1083/jcb.200902142.

811 Persson, L.B., V.S. Ambati, and O. Brandman. 2020. Cellular Control of Viscosity Counters Changes in
812 Temperature and Energy Availability. Cell. 183:1572-1585.e16.
813 doi:10.1016/j.cell.2020.10.017.

814 Peters, L.Z., R. Hazan, M. Breker, M. Schuldiner, and S. Ben-Aroya. 2013. Formation and dissociation
815 of proteasome storage granules are regulated by cytosolic pH. J. Cell Biol. 201:663–671.
816 doi:10.1083/jcb.201211146.

817 Petrovska, I., E. Nüske, M.C. Munder, G. Kulasegaran, L. Malinovska, S. Kroschwald, D. Richter, K.
818 Fahmy, K. Gibson, J.-M. Verbavatz, and S. Alberti. 2014. Filament formation by metabolic

819 enzymes is a specific adaptation to an advanced state of cellular starvation. Elife.
820 doi:10.7554/eLife.02409.

821 Plowman, R., N. Singh, E.C. Tromer, A. Payan, E. Duro, C. Spanos, J. Rappsilber, B. Snel, G.J.P.L. Kops,
822 K.D. Corbett, and A.L. Marston. 2019. The molecular basis of monopolin recruitment to the
823 kinetochore. Chromosoma. 128:331–354. doi:10.1007/s00412-019-00700-0.

824 Rabitsch, K.P., M. Petronczki, J.P. Javerzat, S. Genier, B. Chwalla, A. Schleiffer, T.U. Tanaka, and K.
825 Nasmyth. 2003. Kinetochore recruitment of two nucleolar proteins is required for homolog
826 segregation in meiosis I. Dev Cell. 4:535–548. doi:10.1016/s1534-5807(03)00086-8.

827 Rabouille, C., and S. Alberti. 2017. Cell adaptation upon stress: the emerging role of membrane-less
828 compartments. Curr Opin Cell Biol. 47:34–42. doi:10.1016/j.ceb.2017.02.006.

829 Richmond, D., R. Rizkallah, F. Liang, M.M. Hurt, and Y. Wang. 2013. Slk19 clusters kinetochores and
830 facilitates chromosome bipolar attachment. Mol Biol Cell. 24:566–577. doi:10.1091/mbc.E12-
831 07-0552.

832 Roll-Mecak, A. 2020. The Tubulin Code in Microtubule Dynamics and Information Encoding. Dev Cell.
833 54:7–20. doi:10.1016/j.devcel.2020.06.008.

834 Roostalu, J., C. Hentrich, P. Bieling, I.A. Telley, E. Schiebel, and T. Surrey. 2011. Directional Switching
835 of the Kinesin Cin8 Through Motor Coupling. Science. doi:10.1126/science.1199945.

836 Roostalu, J., and T. Surrey. 2017. Microtubule nucleation: beyond the template. Nat. Rev. Mol. Cell
837 Biol. doi:10.1038/nrm.2017.75.

838 Röper, K. 2020. Microtubules enter centre stage for morphogenesis. Philos Trans R Soc Lond B Biol
839 Sci. 375:20190557. doi:10.1098/rstb.2019.0557.

840 Rutledge, M.T., M. Russo, J.-M. Belton, J. Dekker, and J.R. Broach. 2015. The yeast genome
841 undergoes significant topological reorganization in quiescence. Nucleic Acids Res. 43:8299–
842 8313. doi:10.1093/nar/gkv723.

843 Sagot, I., B. Pinson, B. Salin, and B. Daignan-Fornier. 2006. Actin bodies in yeast quiescent cells: an
844 immediately available actin reserve? Mol. Biol. Cell. 17:4645–4655. doi:10.1091/mbc.E06-04-
845 0282.

846 Sanchez, A.D., and J.L. Feldman. 2017. Microtubule-organizing centers: from the centrosome to non-
847 centrosomal sites. Curr. Opin. Cell Biol. 44:93–101. doi:10.1016/j.ceb.2016.09.003.

848 Schatz, P.J., F. Solomon, and D. Botstein. 1986. Genetically essential and nonessential alpha-tubulin
849 genes specify functionally interchangeable proteins. Mol Cell Biol. 6:3722–3733.
850 doi:10.1128/mcb.6.11.3722-3733.1986.

851 Scholey, J.E., S. Nithianantham, J.M. Scholey, and J. Al-Bassam. 2014. Structural basis for the
852 assembly of the mitotic motor Kinesin-5 into bipolar tetramers. Elife. 3:e02217.
853 doi:10.7554/eLife.02217.

854 Shapira, O., and L. Gheber. 2016. Motile properties of the bi-directional kinesin-5 Cin8 are affected
855 by phosphorylation in its motor domain. Sci Rep. 6:25597. doi:10.1038/srep25597.

856 Shimamoto, Y., S. Forth, and T.M. Kapoor. 2015. Measuring Pushing and Braking Forces Generated by
857 Ensembles of Kinesin-5 Crosslinking Two Microtubules. Dev Cell. 34:669–681.
858 doi:10.1016/j.devcel.2015.08.017.

859 Singh, S.K., H. Pandey, J. Al-Bassam, and L. Gheber. 2018. Bidirectional motility of kinesin-5 motor
860 proteins: structural determinants, cumulative functions and physiological roles. Cell. Mol. Life
861 Sci. 75:1757–1771. doi:10.1007/s00018-018-2754-7.

862 Sirajuddin, M., L.M. Rice, and R.D. Vale. 2014. Regulation of microtubule motors by tubulin isotypes
863 and post-translational modifications. Nat Cell Biol. 16:335–344. doi:10.1038/ncb2920.

864 Thawani, A., and S. Petry. 2021. Molecular insight into how γ-TuRC makes microtubules. J Cell Sci.
865 134:jcs245464. doi:10.1242/jcs.245464.

866 Thomas, G.E., K. Bandopadhyay, S. Sutradhar, M.R. Renjith, P. Singh, K.K. Gireesh, S. Simon, B.
867 Badarudeen, H. Gupta, M. Banerjee, R. Paul, J. Mitra, and T.K. Manna. 2016. EB1 regulates
868 attachment of Ska1 with microtubules by forming extended structures on the microtubule
869 lattice. Nat Commun. 7:11665. doi:10.1038/ncomms11665.

870 Tóth, A., K.P. Rabitsch, M. Gálová, A. Schleiffer, S.B. Buonomo, and K. Nasmyth. 2000. Functional
871 genomics identifies monopolin: a kinetochore protein required for segregation of homologs
872 during meiosis i. Cell. 103:1155–1168. doi:10.1016/s0092-8674(00)00217-8.

873 Weinger, J.S., M. Qiu, G. Yang, and T.M. Kapoor. 2011. A nonmotor microtubule binding site in
874 kinesin-5 is required for filament crosslinking and sliding. Curr Biol. 21:154–160.
875 doi:10.1016/j.cub.2010.12.038.

876 Wheway, G., L. Nazlamova, and J.T. Hancock. 2018. Signaling through the Primary Cilium. Frontiers in
877 Cell and Developmental Biology. 6.

878 Wigge, P.A., O.N. Jensen, S. Holmes, S. Souès, M. Mann, and J.V. Kilmartin. 1998. Analysis of the
879 Saccharomyces spindle pole by matrix-assisted laser desorption/ionization (MALDI) mass
880 spectrometry. J. Cell Biol. 141:967–977.

881 Winey, M., and K. Bloom. 2012. Mitotic spindle form and function. Genetics. 190:1197–1224.
882 doi:10.1534/genetics.111.128710.

883 Yukawa, M., Y. Teratani, and T. Toda. 2020. How Essential Kinesin-5 Becomes Non-Essential in Fission
884 Yeast: Force Balance and Microtubule Dynamics Matter. Cells. 9:E1154.
885 doi:10.3390/cells9051154.

886 Zareiesfandabadi, P., and M.W. Elting. 2022. Force by minus-end motors Dhc1 and Klp2 collapses the
887 S. pombe spindle after laser ablation. Biophysical Journal. 121:263–276.
888 doi:10.1016/j.bpj.2021.12.019.

889 Zeng, X., J.A. Kahana, P.A. Silver, M.K. Morphew, J.R. McIntosh, I.T. Fitch, J. Carbon, and W.S.
890 Saunders. 1999. Slk19p is a centromere protein that functions to stabilize mitotic spindles. J
891 Cell Biol. 146:415–425. doi:10.1083/jcb.146.2.415.

892

893 **Abbreviations**

894 MT: microtubule

895 SPB: spindle pole body

896 GTP: guanosine triphosphate

897 MTOC: microtubule organizing center

898 ɣ-TuC: ɣ-tubulin complex

899 MAPs: microtubule associated proteins

900 Q-nMT bundle: quiescence specific nuclear microtubule bundle

901 CPC : chromosome passenger complex

902

903 ## Figure legends

904 **Figure 1: The formation of the Q-nMT bundle is a three-step process.**

905 **(A)** Nuclear MT length in WT cells expressing mTQZ-Tub1, before (**-**) or after (**+**) a 15 min Noc
906 treatment (30 µg/ml) upon entry into quiescence. Each circle corresponds to the length of an
907 individual MT structure. Three independent experiments are shown (pale blue, cyan and dark
908 blue, n > 160 for each point in each experiment). The mean and SD are shown. Student test or
909 ANOVA (sample >2) were used to compare inter-replicates. #: p-value > 0.05, $: p-value < 0.05.
910 A student test (t-test with two independent samples) was used to compare the results
911 obtained with or without Noc, the indicated p-values being the highest measured among
912 experiments. ***: p-value < 1.10^{-5}. Images of representative cells are shown. Bar is 2 µm.

913 **(B)** MT fluorescence intensity as a proxy of MT structure width in WT cells expressing mTQZ-
914 Tub1. Mean intensity measurement for half pre-anaphase mitotic spindles (purple), phase I
915 (green), phase II (orange) or phase III (red) Q-nMT bundle. A line scan along the MT structure
916 for individual cells are shown as thin lines, the mean as a bold line (n > 60 / phase), all the lines
917 being aligned at 0,5 µm before the fluorescence intensity increase onset on the SPB side. The
918 blue lines are results obtained after a 15 min Noc treatment (30 µg/ml). In each graph,
919 horizontal dashed line indicates the mean intensity. Images in pseudo-colors of a
920 representative cell for each phase are shown. Bar is 2 µm.

921 **(C)** MT bundle length as a function of MT bundle width for individual cells in each phase before
922 and after a 15 min Noc treatment (30 µg/ml) in WT cells expressing mTQZ-Tub1. Each circle
923 represents an individual MT structure.

924 **(D)** WT cells expressing mTQZ-Tub1 (red) and Nuf2-GFP (green) in phase II (23 h) or phase III
925 (50 h) were deposited on an agarose pad containing 30 µg/ml Noc and imaged. Blue

926 arrowheads: SPB; white arrowheads: Nuf2-GFP clusters. Time is in min after deposition on the
927 pad. Bar is 1 µm.
928 **(E)** Tub4-mTQZ fluorescence intensity measured at the SPB upon entry into quiescence. Each
929 circle represents an individual cell. The mean and SD are shown; t-tests were used to compare
930 independent samples (N = 3, n > 150), *: 0.05 > p-value > 1.10^{-3}, ***: p-value < 1.10^{-5}. Images
931 in pseudo-colors of representative cells are shown. Bar is 2 µm.
932 **(F)** WT cells expressing mTQZ-Tub1 under the *TUB1* promoter and mRuby-Tub1 under the
933 *ADH2* promoter. The percentage of cells harboring both mTQZ and mRuby fluorescence along
934 the Q-nMT bundle is shown; each circle being the percentage for an independent experiment,
935 with n > 200 cells counted for each experiment. The mean and SD are shown. Images of
936 representative cells at the indicated time after glucose exhaustion are shown. Bar is 2 µm.
937 **(G)** Schematic of the Q-nMT bundle formation. During phase I, stable MTs (phase I-MT - green)
938 elongate from the SPB (grey). During phase II, the amount of Tub4 (cyan) increases at the SPB.
939 In the meantime, new MTs (phase II-MT - orange) elongated from the SPB and are stabilized
940 along the phase I-MTs, yet their +ends remain dynamic (dashed lines). After phase III, all MTs
941 are stabilized (red). Nuf2 is schematized as dark blue squares.
942 **(H)** Upon glucose exhaustion, WT cells expressing mTQZ-Tub1 (green) and Nuf2-GFP (red)
943 were pulsed treated with 30 µg/ml Noc (blue) or DMSO (grey) for 24 h. Noc or DMSO were
944 then chased using carbon exhausted medium and cells were imaged. Each circle corresponds
945 to MT structure length in an individual cell. The mean and SD are shown (N = 3, n > 100).
946 Images of representative cells 2 d after the chase and representative cells 5 days after the
947 chase are shown. For the right panels, tubulin (green) was detected by immunofluorescence,
948 actin (red) by phalloidin and DNA (blue) with DAPI. The mean Q-nMT bundle length (±SD) in
949 the population is indicated.

950

951 **Figure 2: Q-nMT bundle formation is influenced by the alpha-tubulin amount and isotype**

952 **(A)** WT cells (4 d) expressing either Tub3-3GFP (green) and mTQZ-Tub1 (red, top panel) or
953 Tub3-RFP (red) and mWasabi-Tub1 (green, bottom panel). Blue arrowheads point to SPB, bar
954 is 2 µm.

955 **(B)** Nuclear MT length in WT and *tub3Δ* cells expressing mTQZ-Tub1, 36 h (phase II, orange)
956 and 90 h (phase III, red) after glucose exhaustion, treated 15 min (blue) or not (grey) with 30
957 µg/ml Noc. Each circle corresponds to the length of an individual MT structure, mean and SD
958 are shown. ANOVA was used to compare inter-replicates (n > 200, N = 5); #: p-value > 0.05, $:
959 p-value < 0.05. A student test (t-test with two independent samples) was used to compare (**+**)
960 or (**-**) Noc data. The indicated p-values are the highest calculated among the 5 experiments;
961 ***: p-value < 1.10^{-5}. Images of representative cells are shown, bar is 2 µm.

962 **(C)** Nuclear MT length in WT and *Tub1-only* cells expressing mTQZ-Tub1, 36 h (phase II, orange)
963 and 90 h (phase III, red) after glucose exhaustion, treated 15 min or not with 30 µg/ml Noc.
964 Statistical representations are as in (B). Images of representative cells are shown, bar is 2 µm.

965 **(D)** Fluorescence intensity along the Q-nMT bundle in WT (grey) and *Tub1-only* (blue) cells
966 expressing mTQZ-Tub1 grown for 10 h (phase I), 36 h (phase II), and 90 h (phase III). Individual
967 fluorescent intensity is shown as thin line, the mean as a bold line (n > 60 / phase), all the lines
968 being aligned at 0,5 µm before the fluorescence intensity increase onset on the SPB side.
969 Dashed lines indicate the maximal mean fluorescence intensity. Images in pseudo-color of
970 representative cells are shown, bar is 2 µm.

971

972 **Figure 3: Kinetochore-kinetochore interactions are required for Q-nMT bundle formation.**

973 **(A)** Nuclear MT length distribution in WT (grey) and *ndc80-1* (violet) cells expressing mTQZ-
974 Tub1 (green) and Nuf2-GFP (red), transferred to 37 °C upon glucose exhaustion and
975 maintained at 37 °C for the indicated time. Cells were imaged after a 20 min Noc treatment
976 (30 µg/ml). See Sup. Fig. 3B for the control without Noc. Each circle corresponds to the length
977 of an individual MT structure, mean and SD are shown. A student test (t-test with two
978 independent samples) was used to compare (**+**) or (**-**) Noc samples from the same experiment
979 (n > 250, N = 2). The indicated p-values are the highest p-values calculated among the 2
980 repeated experiments. ***: p-value < 1.10^{-5}. Images of representative cells incubated 12 h at
981 37 °C are shown, bar is 2 µm.
982 **(B)** WT (grey) and *ipl1-5as* (pink) cells expressing mTQZ-Tub1 were treated for 60 h with 50
983 µM NA-PP1 after glucose exhaustion, and imaged after a 15 min Noc treatment (30 µg/ml),
984 see Sup. Fig. 3D for control without Noc. Same statistical representation as in (A); N = 2, n >
985 250. Images of representative cells are shown, bar is 2 µm.
986 **(C)** WT cells (2 d) expressing mTQZ-Tub1 (red) and Bir1-GFP or Sli15-GFP (green) were imaged.
987 Graphs show Bir1-GFP or Sli15-GFP fluorescence intensity along normalized Q-nMT bundles
988 (see material and method section, plain and dash lines: mean and SD respectively). Images of
989 representative cells are shown, bar is 2 µm.
990 **(D)** Nuclear MT length distribution in cells of the indicated genotype (4 d) expressing mTQZ-
991 Tub1 treated or not with Noc (30 µg/ml). Same statistical representation as in (A); N = 3, n >
992 200. Images of representative cells are shown, bar is 2 µm.
993 **(E)** WT cells expressing mTQZ-Tub1 (red) and Slk19-GFP (green) 4 h after glucose exhaustion.
994 Blue arrowhead: SPB, bar is 2 µm.
995 **(F)** Nuclear MT length distribution in cells of the indicated genotype (4 d) expressing mTQZ-
996 Tub1 (green) and Nuf2-GFP (red) imaged before or after Noc treatment (30 µg/ml). Same

997 statistical representation as in (A); N = 2, n > 200. Images of representative cells are shown.
998 White arrowheads point to Nuf2-GFP dots, bar is 2 µm.
999 **(G)** Cells of the indicated genotype (4 d) expressing mTQZ-Tub1 (green) and Nup2-RFP (red),
1000 bar is 1 µm.
1001 **(H)** Nuclear MT length distribution in cells of the indicated genotype (4 d) expressing mTQZ-
1002 Tub1 treated or not with Noc (30 µg/ml). Same statistical representation as in (A); N ≥ 2, n >
1003 200. Images of representative cells are shown, bar is 2 µm.
1004 **(I)** Length variation of nuclear MT bundle fragments after laser ablation (pink dash line) in cells
1005 expressing mRuby-TUB1 (red) and Dad2-GFP (green). Time is in min. Images of representative
1006 cells are shown, blue arrowhead: SPB, white arrowhead: cMT. Graph indicates the variation
1007 of length in released fragments (n > 120) and histograms show the % of released or SBP
1008 attached fragments that are either stable, or that shorten or grow within a 30 min period after
1009 the laser-induced breakage. Bar is 1 µm
1010
1011 **Figure 4: Each phase of Q-nMT formation requires a specific kinesin.**
1012 **(A)** Images of representative WT cells (2 d) expressing Kar3-3GFP (green) and mTQZ-Tub1 (red)
1013 and corresponding fluorescence intensity along normalized Q-nMT bundles (see material and
1014 method section), bar is 2 µm.
1015 **(B)** Morphometric Q-nMT bundle properties distribution in 4 d WT (grey), *kar3Δ* (red), *vik1Δ*
1016 (blue), and *cik1Δ* cells (green) expressing mTQZ-Tub1 after Noc treatment (30 µg/ml) – see
1017 Sup. Fig. 4A for the control without Noc. Each circle corresponds to an individual Q-nMT
1018 bundle. Black crosses are mean and SD. Images of representative cells are shown, bar is 2 µm.
1019 **(C)** Nuclear MT length distribution in WT and *cin8Δ* cells expressing mTQZ-Tub1 treated (**+**) or
1020 not (**-**) with 15 min Noc (30 µg/ml). Each circle corresponds to the length of an individual MT

1021 structure, mean and SD are shown. A student test (t-test with two independent samples) was
1022 used to compare (**+**) or (**-**) Noc samples from the same experiment (n > 250, N = 2). The
1023 indicated p-values are the highest p-values calculated among the 2 repeated experiments.
1024 ***: p-value < 1.10^{-5}.
1025 **(D)** Fluorescence intensity along Q-nMT bundles in WT and *cin8Δ* cells expressing mTQZ-Tub1
1026 7 h and 24 h after glucose exhaustion. Thin line: intensity from an individual cell; bold line:
1027 mean intensity (n > 60 / phase). Images of representative cells are shown. Bar is 2 µm.
1028 **(E)** WT and *cin8Δ* cells expressing mEOS3.2-Tub1 were imaged using PALM Images in pseudo-
1029 colors of representative cells are shown. Full width at half maximum (FWHM) was measured
1030 at the indicated distance from the SPB. Each line in the bottom graphs corresponds to a single
1031 cell; p-value between WT and *cin8Δ* are indicated (unpaired T-test). Bar is 1 µm.
1032 **(F)** Images of representative WT cells (3 d) expressing Kip1-GFP (green) and mTQZ-Tub1 (red).
1033 Graphs show fluorescence intensity along normalized Q-nMT bundles (plain and dash lines:
1034 mean and SD respectively). Bar is 2 µm, blue arrowhead: SPB.
1035 **(G)** Representative images of WT, *kip1Δ* and *kip3Δ* cells expressing mTQZ-Tub1 treated (**+**) or
1036 not (**-**) with 15 min Noc (30 µg/ml), Bar is 2 µm.
1037 **(H)** Nuclear MT length distribution in WT, *kip1Δ* and *kip3Δ* cells expressing mTQZ-Tub1 treated
1038 (**+**) or not (**-**) 15 min with Noc (30µg/ml). Legend is the same as in (C); n > 250, N = 2; *: p-value
1039 < 1.10^{-3}; ***: p-value < 1.10^{-6}. MT mean length and SD are indicated.
1040
1041 **Figure 5: Q-nMT bundle disassembly always occurs before SPB separation upon quiescence**
1042 **exit.**
1043 **(A)** WT cells expressing Spc42-RFP (red) (5 d) were re-fed on an YPDA microscope pad.
1044 Individual Q-nMT bundles were measured in cells expressing Nuf2-GFP treated DMSO (top

1045 panel, n=33) or in cells expressing Stu2-GFP treated with CHX (bottom panel, n=49). Each line
1046 corresponds to an individual cell. In the upper panel, time was set to zero at the onset of MT
1047 bundle depolymerisation. In the lower panel, time was set to zero when cells were deposited
1048 on the agarose pad. Images of representative cells are shown, bar is 2 µm

1049 **(B)** Q-nMT bundle length (green) and fluorescence intensity at full width half maximum
1050 (FWHM - orange) were measured upon quiescence exit in WT cells (5 d) expressing mTQZ-
1051 Tub1. Representative example of shrinking Q-nMT bundle is shown on the left, bar is 1 µm.

1052 **(C)** Cells of the indicated genotype expressing mTQZ-Tub1 were grown for 4 d, and re-fed. Q-
1053 nMT bundle length was measured at the indicated time points, 15 min after a Noc treatment
1054 (30 µg/ml), to remove dynamic cMTs that assemble upon quiescence exit. Each circle
1055 corresponds to a single cell. MT mean length and SD are indicated. A student test (t-test with
1056 two independent samples) was used to compare samples from the same experiment (n > 250,
1057 N = 4). The indicated p-values are the highest p-value calculated among the 4 repeated
1058 experiments. ***: p-value < 1.10^{-5}. MT mean length and SD are indicated. Images of
1059 representative 4-day-old cells of the indicated genotype expressing mTQZ-Tub1 before and 60
1060 min after quiescence exit are shown, bar is 2 µm.

1061 **(D)** Representative images of a *kip3Δ* cell expressing Nuf2-GFP upon quiescence exit. Blue and
1062 white arrowheads: SPBs and Q-nMT bundle extremities respectively, bar is 2 µm.

1063 **(E)** Percentage of 6-day-old WT or *kip3Δshe1Δ* cells expressing Spc42-mRFP1 with separated
1064 SPB as a function of time upon quiescence exit (n > 200).

1065 **(F)** WT and *kip3Δshe1Δ* cells (6 d) expressing Spc42-mRFP1 (red) and mTQZ-Tub1 (green) were
1066 re-fed on a YPDA microscope pad. Percentage of cells with a single SBP with or without Q-nMT
1067 bundle or with duplicated SPBs were scored (N = 4, n > 200), SD are indicated. Images of

1068 representative cells are shown, bar is 2 µm. Right bottom panel: actin (phalloidin staining, red)
1069 in *kip3Δ she1Δ* cells (6 d) expressing mTQZ-Tub1 (green) before and 1 h after quiescence exit.
1070

1071 **Figure 6: Model for Q-nMT bundle assembly**

1072 (a) In G1, the nucleus is in a Rabl-like configuration. (b) Upon quiescence establishment,
1073 chromosomes get condensed. MT-kinetochore interaction and Ilp1 are required for the onset
1074 of phase I. (c) Kar3 and its regulator Cik1 are essential to initiate Q-nMT bundle elongation.
1075 Although deletion of *BIM1* has no effect, it becomes critical for phase I if kinetochore-MT
1076 interactions are destabilized by the absence of Chromosome Passenger Complex components.
1077 Kinetochore clustering by the monopolin complex and Slk19 is needed to maintain MT
1078 bundling while phase I-MTs elongate. During phase I, Tub4 accumulates at the SPB. (d) In
1079 phase II, a second wave of MT nucleation and elongation occurs. Phase II-MTs are concurrently
1080 stabilized along pre-existing phase I-MTs, in a Cin8-dependent manner. Phase I and phase II
1081 MTs +ends (>1 µm) remain dynamic until the full-length Q-nMT bundle stabilization is reached
1082 via the action of Kip1, about 2 days after glucose exhaustion (e).

1083

1084 ## Supplementary Figure legends

1085 **Supplementary Figure 1**

1086 **(A)** Fluorescence intensity along MT structures in WT cells expressing mTQZ-Tub1. Mean
1087 intensity measurement for half pre-anaphase mitotic spindles (violet, n = 60), phase I (green,
1088 n = 19), and phase II (orange, n= 22) Q-nMT bundles. A line scan along the MT structure for an
1089 individual cell is shown as thin line, the mean as a bold line, all the lines being aligned at 0,5
1090 µm before the fluorescence intensity increase onset on the SPB side.

1091 **(B)** Individual Q-nMT bundle full width measured at half-maximum in WT cells (4 d) expressing
1092 mTQZ-Tub1 before or after 1 h after Noc treatment. A paired t-test was use to compare the
1093 two conditions (n > 40).

1094 **(C)** Nuclear MT length in WT haploid (mat a and mat α) or diploid (mat a/mat α) cells
1095 expressing mTQZ-TUB1. Each circle represents an individual cell. Mean and SD are shown in
1096 red.

1097 **(D)** Nuclear MT length in WT proliferating cells expressing mTQZ-Tub1 transferred to water
1098 for the indicated time and treated (**+**) or not (**-**) 15 min with 30 µg/ml Noc. Images of
1099 representative cells are shown, bar is 2 µm.

1100 **(E)** WT cells expressing Spc42-RFP (red) and mTQZ-Tub1 (green, top panel) or Nuf2-GFP
1101 (green, bottom panel) upon entry into quiescence. The percentages indicate the relative
1102 amount of Nuf2-GFP detected at the SBP (blue arrowhead), bar is 1 µm.

1103 **(F)** Tub4-mTQZ fluorescence intensity in WT cells of the W303 background. The mean and SD
1104 are shown; t-test was used to compare independent samples (N = 3, n > 150), ***: p-value <
1105 1.10^{-5}.

1106 **(G)** Fluorescence intensities in WT cells (4 d) expressing Tub4-mTQZ and mRuby-Tub1. The
1107 Tub4-mTQZ signal at the SBP is plotted as a function of the mRuby signal along the Q-nMT
1108 bundle. Each circle represents an individual cell (n = 60).
1109 **(H) Top panel:** western blot using anti-GFP and anti-RFP antibodies on total protein extracts
1110 obtained from the indicated cells upon entry into quiescence. Anti-Ade13 antibodies were
1111 used as loading control. **Bottom panel**: images of representative WT cells expressing only
1112 pTUB1-mTQZ-Tub1 (green) or only pADH2-mRuby-Tub1 (red) upon entry into quiescence as a
1113 control of cross channel fluorescence, bar is 2 µm.
1114 **(I)** WT cells expressing mRuby-Tub1 (4 d) displaying both dynamic cMTs (red arrowhead) and
1115 a Q-nMT bundle (time is in min, bar is 1 µm).
1116 **(J)** An artificial fluid to solid-like phase transition in proliferating cells does not induce MT
1117 stabilization. Proliferating WT cells expressing mTQZ-Tub1 (green) and Spc42-RFP (red) with
1118 fluid (pH = 7.5) or solid-like (pH = 4) cytoplasm/nucleoplasm (see materials and method) were
1119 incubated 15 min with 30 µg/ml Noc (left) or stained with phalloidin to detect actin (right).
1120 Indicated phenotypes were quantified (left and right graphs, N = 2, n > 115, mean and SD are
1121 indicated). Bar is 2 µm.
1122 **(K)** Cells can assemble dynamic cMTs (red arrowhead) in quiescence. 2-day-old WT cells
1123 expressing mRuby-Tub1 were imaged after a 15 min Noc pulse-chase (30 µg/ml, time is in
1124 min). Red arrowhead: cytoplasmic MT, blue arrowhead: SBP, bar is 2 µm.
1125 **(L) Left graphs:** WT cell viability after a 24h-pulse (grey rectangle) with Noc (30 µg/ml, circles)
1126 or DMSO (triangles), followed by a chase using carbon exhausted medium, the Noc pulse being
1127 done either upon glucose exhaustion or 5 days after glucose exhaustion. Each circle/triangle
1128 is the percentage obtained for an independent experiment in which n > 200 cells were scored.
1129 **Right graph:** live cells, as attested by a clear staining after a methylene blue treatment, were

1130 micro-separated 8 days after the Noc pulse done either upon glucose exhaustion or 5 d after
1131 glucose exhaustion, and allowed to give rise to a colony on a YPDA plate. Each circle/triangle
1132 is the percentage obtained for an independent experiment in which n > 100 cells were micro-
1133 separated. Images of representative YPDA plates after 3 d of growth at 30°C are shown.
1134
1135 **Supplementary Figure 2**
1136 **(A)** Expansion microscopy images of WT cells (4 d) expressing Tub3-3GFP and immuno-stained
1137 with GFP (green) and α-tubulin (red) YOL1/2 antibodies, bar is 1 µm.
1138 **(B)** Western blot using α-tubulin YOL1/2 antibody on total protein extracts from the indicated
1139 cells grown for 4 d. Actin was used as a loading reference. Numbers indicate the tubulin/actin
1140 ratio (mean for N = 8).
1141 **(C)** Nuclear MT length in WT, *tub3Δ* and tub1-only cells expressing mTQZ-Tub1, treated or not
1142 with 30 µg/ml Noc. The three independent experiments used in Fig. 2B and Fig. 2C are shown.
1143 P-values for Anova or unpaired t-test are indicated, ***: p-value < 1.10^{-5}.
1144 **(D)** Nuclear MT length distribution in *yke2Δ*, *pac10Δ* or *gim3Δ* cells (4 d) and in corresponding
1145 WT cells expressing Nuf2-GFP (dark grey bars) or Bim1-3GFP (light grey bars). Right panel:
1146 western blot using an anti-α-tubulin antibody on total protein extracts from cells of the
1147 indicated genotype (4 d). Actin was used as a loading reference. The tubulin/actin ratio is
1148 indicated (mean of N=4). Bar is 2 µm.
1149 **(E)** Nuclear MT length distribution in *pac2Δ*, *cin2Δ* or *cin4Δ* cells (4 d) and in corresponding WT
1150 cells expressing Bim1-GFP (dark grey bars). Right panel: western blot using an anti-α-tubulin
1151 antibody on total protein extracts from cells of the indicated genotype (4 d). Actin was used
1152 as a loading reference. The tubulin/actin ratio is indicated (mean for N=4). Bar is 2 µm.
1153

1154 **Supplementary Figure 3**

1155 **(A) Upper panel:** WT cell (4 d) expressing Dad2-GFP and immuno-stained with GFP (green)
1156 and α-tubulin (red) YOL1/2 antibodies imaged using expansion microscopy. Blue is DAPI.
1157 **Lower panel:** WT cell (4 d) expressing Dad2-GFP (green) and mRuby-Tub1 (red), imaged using
1158 SIM. Bar is 1 µm.

1159 **(B)** Nuclear MT length distribution in cells of the indicated genotypes, grown for 3 d at 25 °C,
1160 shifted to 37 °C or 25° C for 48 h, and treated 15 min or not with 30 µg/ml Noc. Each circle
1161 corresponds to the length of an individual MT structure, mean and SD are shown. ***: p-value
1162 $< 1.10^{-6}$. Images of representative cells are shown, bar is 2 µm.

1163 **(C)** WT (grey) and *ipl1-1* cells (pink) expressing mTQZ-Tub1 were shifted upon glucose
1164 exhaustion to 37 °C for 48 h, and imaged after a 20 min Noc treatment (30 µg/ml). Same
1165 legend as in (B). Images of representative cells are shown, bar is 2 µm.

1166 **(D)** Nuclear MT length in cells of the indicated genotypes, grown for 60 h in DMSO or 50 µM
1167 NA-PP1, treated 15 min or not with 30 µg/ml Noc. Same legend as in (B). Images of
1168 representative cells are shown, bar is 2 µm.

1169 **(E)** Western blot using anti-myc antibodies on total protein extracts from cells expressing *ipl1-*
1170 *5as*-myc treated 60 h with DMSO or 50 µM NA-PP1 after quiescence entry. Ade13 was used
1171 as a loading reference.

1172 **(F)** Nuclear MT length in cells of the indicated genotypes grown 48 h at 37 °C or 96 h at 25 °C,
1173 treated 15 min or not with 30 µg/ml Noc. Same legend as in (B). Images of representative cells
1174 are shown, bar is 2 µm.

1175 **(G)** Distribution of Bim1-3GFP intensity as a function of mTQZ-Tub1 intensity in individual Q-
1176 nMT bundles (green: phase I – 7 h after glucose exhaustion, orange: phase II – 26 h after

1177 glucose exhaustion and red: phase III – 50h after glucose exhaustion). Each circle represents
1178 an individual Q-nMT bundle.

1179 **(H)** Viability (methylene blue staining) after the indicated time in quiescence (left graph),
1180 capacity to form colony after single live cell micro-manipulation after 12 days in quiescence
1181 (right graph). Pictures of representative plates 3 d after cell micro-manipulation are shown.

1182 **(I)** Western blot using anti-GFP antibodies on total protein extracts from proliferating or 4-
1183 days-old cells expressing the indicated GFP fusion protein. Ade13 and Act1 were used as
1184 loading controls.

1185 **(J)** Percentage of cells of the indicated genotype displaying a MT star-like array. Each circle
1186 represents the % obtained for an independent culture (n > 200). Mean and SD are indicated.

1187 **(K)** WT cells (6 d) expressing mRuby-Tub1 (red) and Nuf2-GFP (green) were transferred onto
1188 an agarose pad. Q-nMT bundles were cut using a pulsed laser (pink dashed line). White
1189 arrowheads point to dynamic cMTs. Time is in min, bar is 2 µm.

1190 **(L)** Proliferating cells expressing mRuby-Tub1 (red) and Dad2-GFP (green) were transferred
1191 onto an agarose pad. Anaphase spindles were cut and the behavior of the released fragments
1192 was followed. Time is in min, bar is 2 µm.

1193 **(M)** Nuclear MT length in cells of the indicated genotypes, grown for 3 d at 25 °C, shifted to
1194 37 °C or 25° C for 48 h, and treated 15 min or not with 30 µg/ml Noc. Same legend as in (B).
1195 Images of representative cells are shown, p-value from unpaired t-test is indicated, bar is 2
1196 µm.

1197

1198 **Supplementary Figure 4**

1199 **(A)** Q-nMT bundle length as a function of Q-nMT bundle width for individual WT cells (grey)
1200 and *kar3Δ* cells (red) 90 h after glucose exhaustion.
1201 **(B)** WT cells expressing mTQZ-Tub1 (red) and Cin8-GFP (green) were imaged at the indicated
1202 times after glucose exhaustion. Cells expressing only mTQZ-Tub1 (left panel) testify for the
1203 absence of fluorescence leak from the mTQZ signal into the GFP channel. Bar is 2µm.
1204 **(C)** Fluorescence intensity along Q-nMT bundles in WT (black) and *cin8Δ* cells expressing
1205 mTQZ-Tub1, treated (green) or not (red) with Noc. Each line is an individual cell, the bold lines
1206 are the mean (n > 20).
1207 **(D)** Morphometric Q-nMT bundle properties distribution in WT (grey) and *cin8Δ* (green) cells
1208 expressing mTQZ-Tub1. Each circle is an individual cell.
1209 **(E)** Fluorescence intensity along Q-nMT bundles in WT (grey, n > 50), *kip1Δ* (red, n > 50), *bim1Δ*
1210 (green, n > 50), and *kip1Δ bim1Δ* (blue, n > 30) cells (4 d). Each line is an individual cell, the
1211 bold lines are the mean.
1212 **(F)** Nuclear MT length distribution in *kip2Δ* cells expressing mTQZ-Tub1 treated 15 min (blue
1213 dots) or not (black dots) with 30 µg/ml Noc. For a comparison, the mean WT length is indicated
1214 as dashed line. Unpaired t-test p-values are indicated.
1215
1216 **Supplementary Figure 5**
1217 **(A)** Representative 5-day-old cells (left and right) expressing mTQZ-Tub1 (red) and Nuf2-GFP
1218 (green) exiting quiescence on a YPDA agarose pad. Blue arrowhead: SBP; white arrows Nuf2-
1219 GFP clusters. Time is in min, bar is 1µm.
1220 **(B)** WT and *kip3Δ* cells (5 d) expressing Nuf2-GFP were re-fed on an YPDA microscope pad.
1221 Each line corresponds to an individual cell. Data were presented either (left) with the time set

1222 to zero at the onset MT depolymerisation or (right) at the onset of SPB separation (red dash
1223 line).
1224 **(C)** Western blot using GFP antibodies on total protein extracts from WT cells expressing Kip3-
1225 GFP grown for the indicated time. Sac6 was used as a loading control.

1226 **(D-E)** Nuclear Q-nMT bundle length in cells of the indicated genotype expressing mTQZ-Tub1,
1227 grown for 4 d and imaged at the indicated time after refeeding. For the rapamycin experiment
1228 in (D), WT cells were pre-incubated 1 h with rapamycin (1 µg/mL), and then re-fed in presence
1229 of the drug. For thermo-sensitive strains in (E), cells were grown 4 d at 25 °C, shifted 1 h at 37
1230 °C, and then transferred to new medium at 37 °C to trigger quiescence exit. Measurements
1231 were done after a 15 min Noc treatment (30 µg/ml) to remove dynamic cMTs. Each circle
1232 represents an individual cell. Mean and SD are indicated.
1233 **(F-G)** Nuclear Q-nMT bundle length in cells of the indicated genotype expressing mTQZ-Tub1
1234 grown for the indicated time at 25 °C, shifted to 37 °C and re-fed. In G, measurements were
1235 done after a 15 min Noc treatment (30 µg/ml) to remove dynamic cMTs. Each circle represents
1236 an individual cell. Mean and SD are indicated.
1237 **(H)** 3 individual experiments in which nuclear MT length was measured in 4-day-old
1238 *kip3Δshe1Δ* cells expressing mTQZ-Tub1 upon quiescence exit (n > 100). P-values from
1239 unpaired t-test are shown. Each circle represents an individual cell. Mean and SD are
1240 indicated.
1241 **(I)** Percentage of cells with separated SPBs upon quiescence exit on YPDA agarose pad (N = 4,
1242 n > 200, left panel). Right: proliferation of WT and *kip3Δshe1Δ* strains in YPDA (OD 600nm as
1243 function of time).
1244 **(J)** Q-nMT bundle length distribution in WT (grey) or *kip3Δshe1Δ* (green) cells with
1245 unseparated SPBs, 240 min after quiescence exit.

1246 **(K)** Actin (red, phalloidin-staining) in WT and *kip3Δshe1Δ* cells expressing mTQZ-TUB1 (green)

1247 at the indicated time upon quiescence exit. Bar is 2µm.

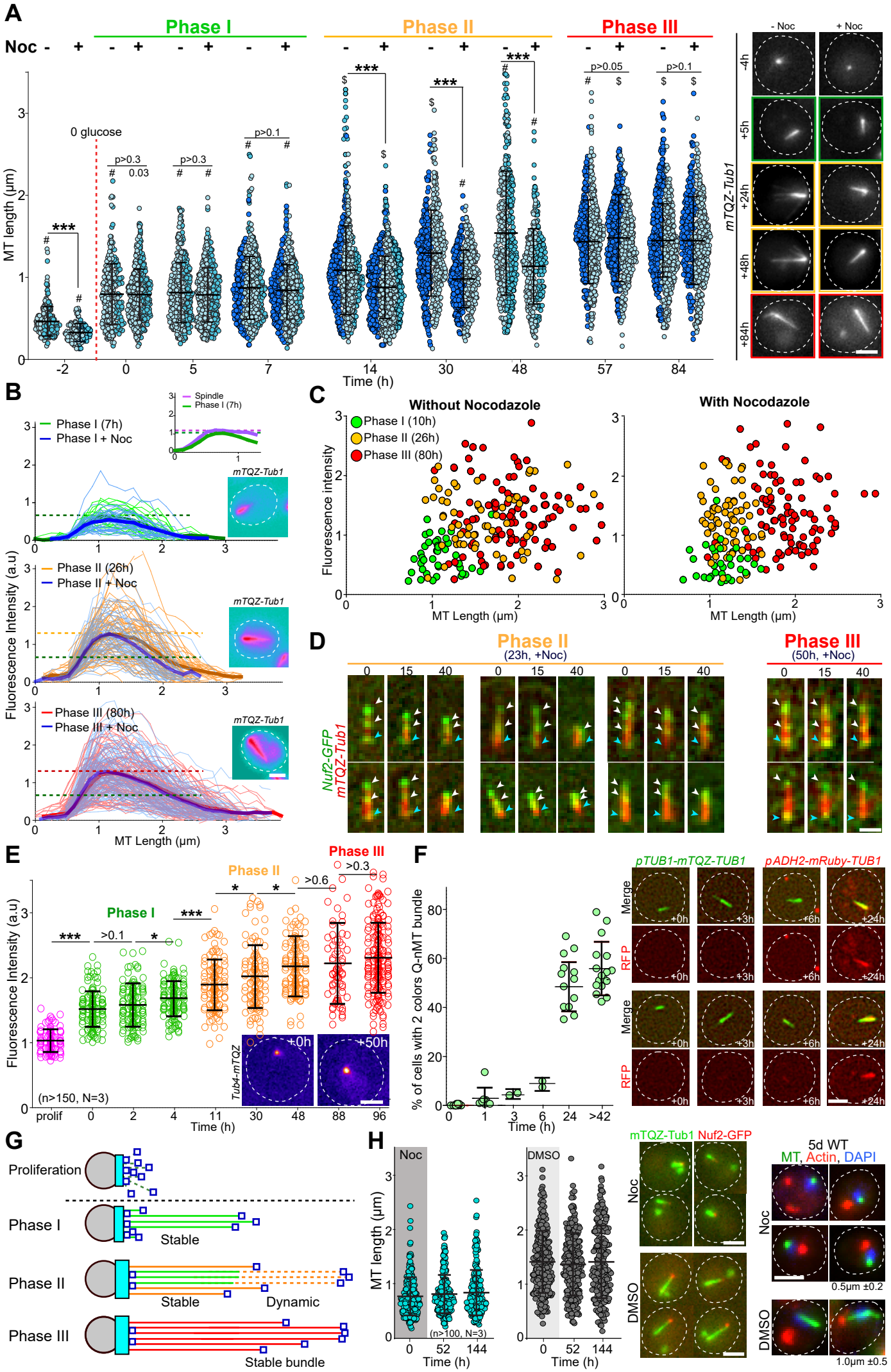
A
Phase I
Phase II
Phase III
Noc - + - + - + - + - + - + - + - + - + - +
MT length (µm)
0 glucose
p>0.3
0.03
p>0.1
p>0.05
***
Time (h)
-2
0
5
7
14
30
48
57
84
- Noc
+ Noc
mTQZ-Tub1
-4h
+5h
+24h
+48h
+84h
B
Phase I (7h)
Phase I + Noc
Spindle
Phase I (7h)
mTQZ-Tub1
Phase II (26h)
Phase II + Noc
Phase III (80h)
Phase III + Noc
Fluorescence Intensity (a.u)
MT Length (µm)
C
Without Nocodazole
With Nocodazole
Phase I (10h)
Phase II (26h)
Phase III (80h)
Fluorescence intensity
MT Length (µm)
D
Phase II
(23h, +Noc)
Phase III
(50h, +Noc)
0
15
40
Nuf2-GFP
mTQZ-Tub1
E
Phase I
Phase II
Phase III
Fluorescence Intensity (a.u)
>0.1
>0.3
>0.6
(n>150, N=3)
Tub4-mTQZ
+0h
+50h
prolif
Time (h)
F
% of cells with 2 colors Q-nMT bundle
Time (h)
pTUB1-mTQZ-TUB1
pADH2-mRuby-TUB1
Merge
RFP
+0h
+3h
+6h
+24h
G
Proliferation
Phase I
Stable
Phase II
Stable
Dynamic
Phase III
Stable bundle
H
Noc
DMSO
MT length (µm)
(n>100, N=3)
Time (h)
mTQZ-Tub1 Nuf2-GFP
5d WT
MT, Actin, DAPI
0.5µm ±0.2
1.0µm ±0.5

Figure 1

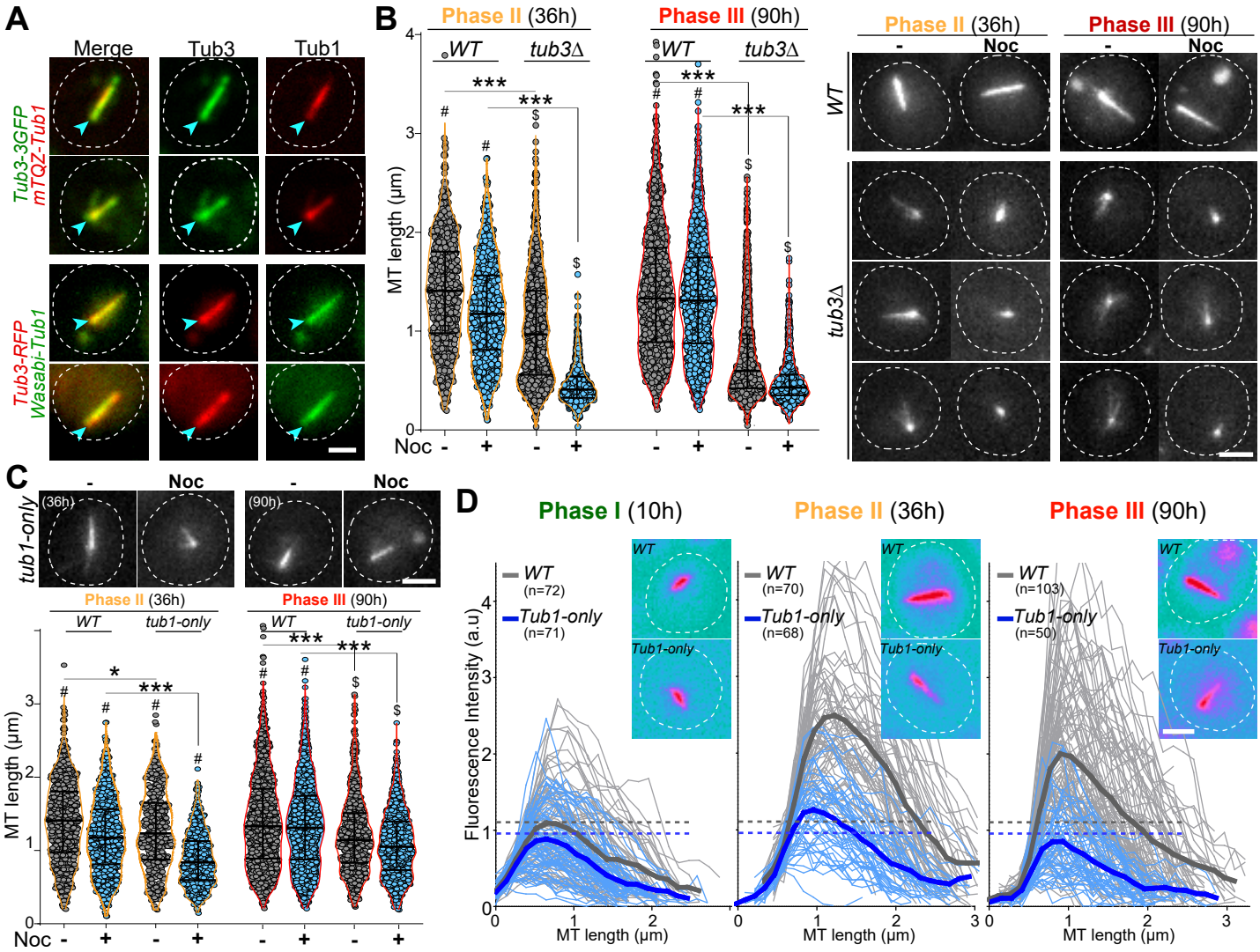
A
Merge
Tub3
Tub1
Tub3-3GFP
mTQZ-Tub1
Tub3-RFP
Wasabi-Tub1
B
Phase II (36h)
Phase III (90h)
WT
tub3Δ
MT length (µm)
Noc
Phase II (36h)
Phase III (90h)
Noc
WT
tub3Δ
C
tub1-only
(36h)
(90h)
Noc
Phase II (36h)
Phase III (90h)
WT
tub1-only
MT length (µm)
Noc
D
Phase I (10h)
Phase II (36h)
Phase III (90h)
WT
(n=72)
Tub1-only
(n=71)
(n=70)
(n=68)
(n=103)
(n=50)
Fluorescence Intensity (a.u)
MT length (µm)

Figure 2

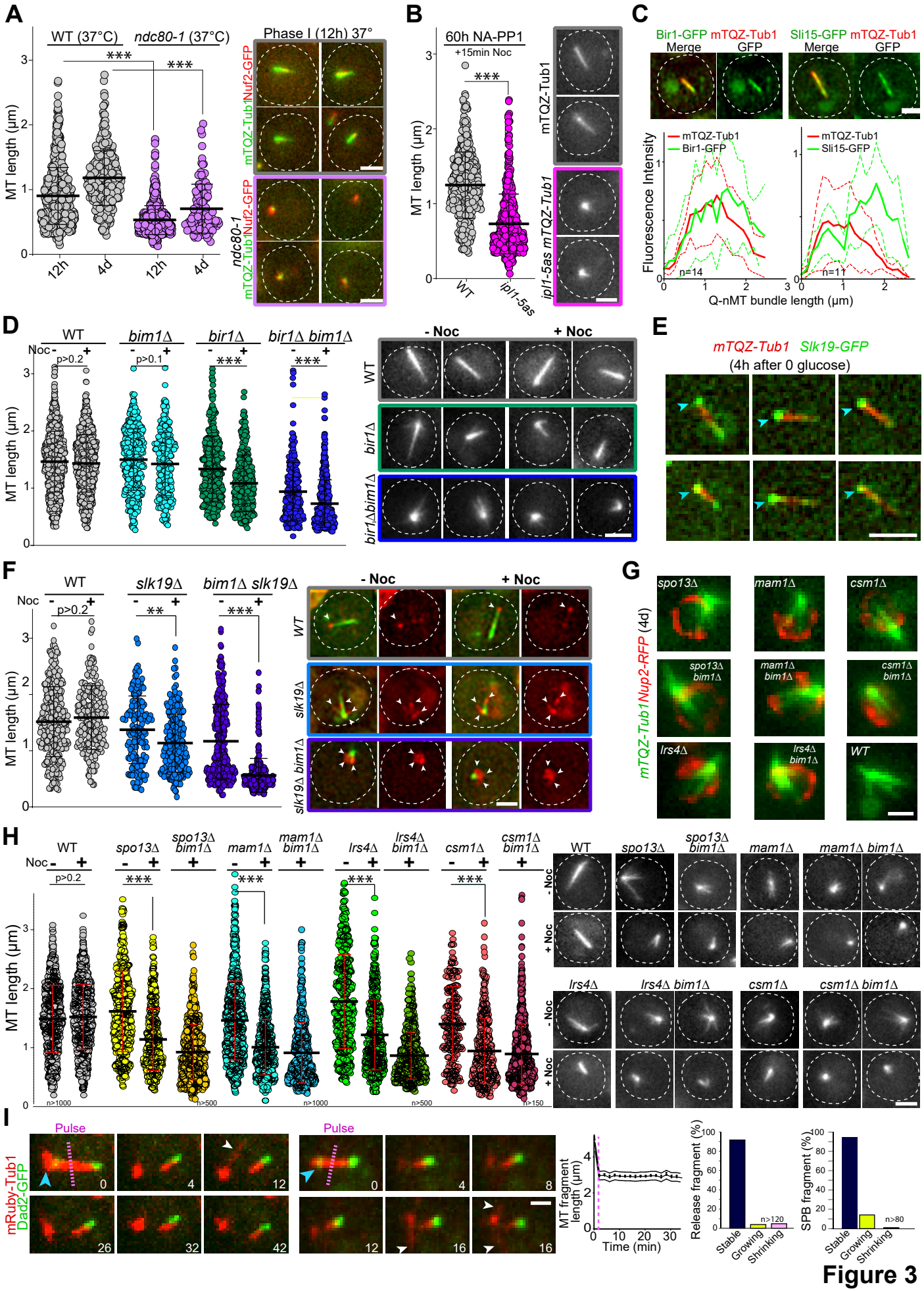
A
WT (37°C)
ndc80-1 (37°C)
Phase I (12h) 37°
MT length (µm)
12h
4d
mTQZ-Tub1Nuf2-GFP
ndc80-1
B
60h NA-PP1
+15min Noc
WT
ipl1-5as
mTQZ-Tub1
ipl1-5as mTQZ-Tub1
C
Bir1-GFP mTQZ-Tub1
Sli15-GFP mTQZ-Tub1
Merge
GFP
Fluorescence Intensity
Q-nMT bundle length (µm)
D
WT
bim1Δ
bir1Δ
bir1Δ bim1Δ
Noc
- Noc
+ Noc
bir1Δbim1Δ
E
mTQZ-Tub1 Slk19-GFP
(4h after 0 glucose)
F
slk19Δ
bim1Δ slk19Δ
slk19Δ bim1Δ
G
spo13Δ
mam1Δ
csm1Δ
spo13Δ bim1Δ
mam1Δ bim1Δ
csm1Δ bim1Δ
lrs4Δ
lrs4Δ bim1Δ
mTQZ-Tub1Nup2-RFP (4d)
H
spo13Δ bim1Δ
mam1Δ bim1Δ
csm1Δ bim1Δ
lrs4Δ bim1Δ
I
Pulse
mRuby-Tub1
Dad2-GFP
MT fragment length (µm)
Time (min)
Release fragment (%)
SPB fragment (%)
Stable
Growing
Shrinking

Figure 3

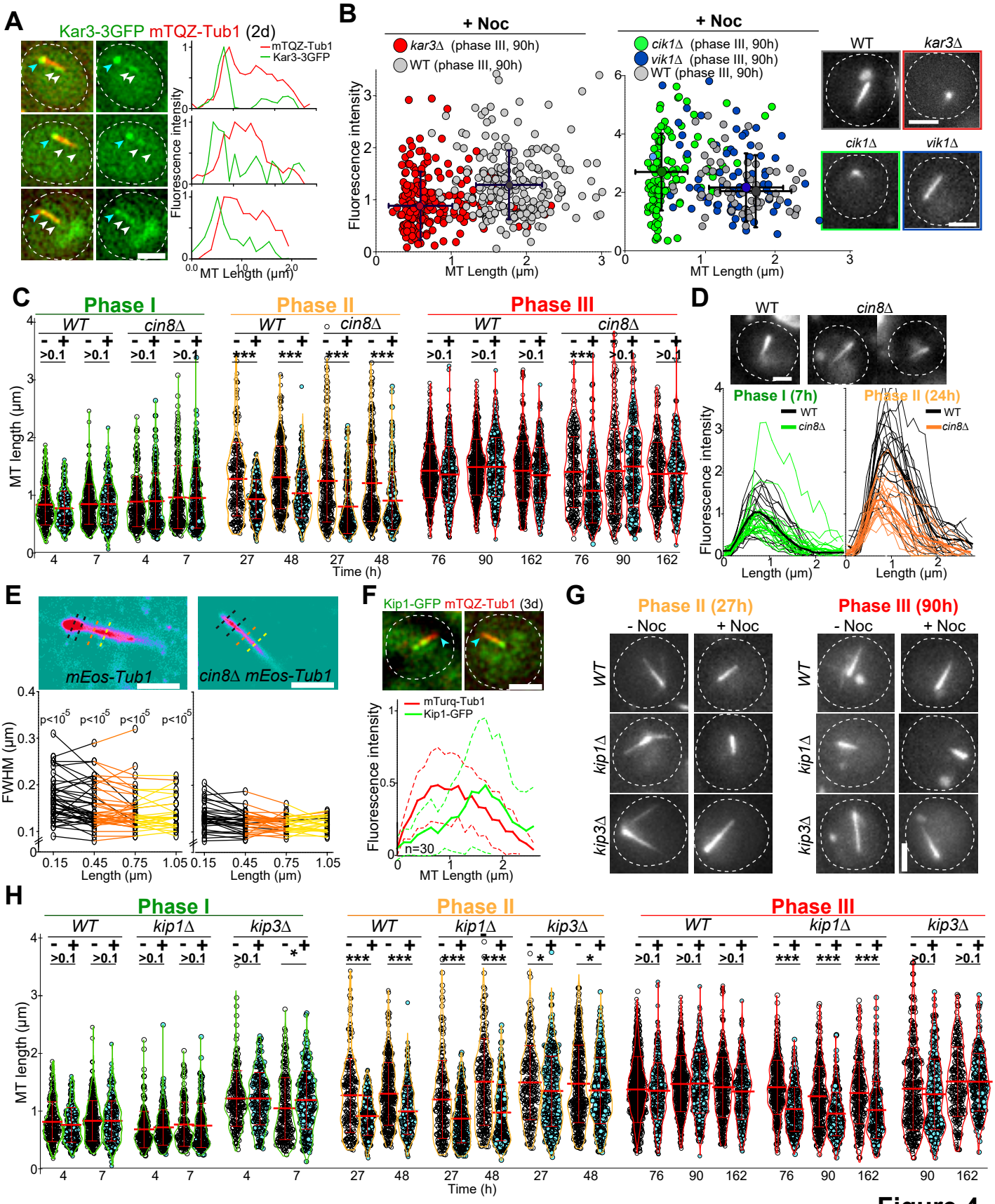
A
Kar3-3GFP mTQZ-Tub1 (2d)
mTQZ-Tub1
Kar3-3GFP
Fluorescence intensity
MT Length (µm)
B
+ Noc
kar3Δ (phase III, 90h)
WT (phase III, 90h)
+ Noc
cik1Δ (phase III, 90h)
vik1Δ (phase III, 90h)
WT (phase III, 90h)
Fluorescence intensity
MT Length (µm)
WT
kar3Δ
cik1Δ
vik1Δ
C
Phase I
Phase II
Phase III
WT
cin8Δ
MT length (µm)
Time (h)
D
WT
cin8Δ
Phase I (7h)
Phase II (24h)
Fluorescence intensity
Length (µm)
E
mEos-Tub1
cin8Δ mEos-Tub1
FWHM (µm)
Length (µm)
F
Kip1-GFP mTQZ-Tub1 (3d)
mTurq-Tub1
Kip1-GFP
Fluorescence intensity
n=30
MT Length (µm)
G
Phase II (27h)
Phase III (90h)
- Noc
+ Noc
WT
kip1Δ
kip3Δ
H
Phase I
Phase II
Phase III
WT
kip1Δ
kip3Δ
MT length (µm)
Time (h)

Figure 4

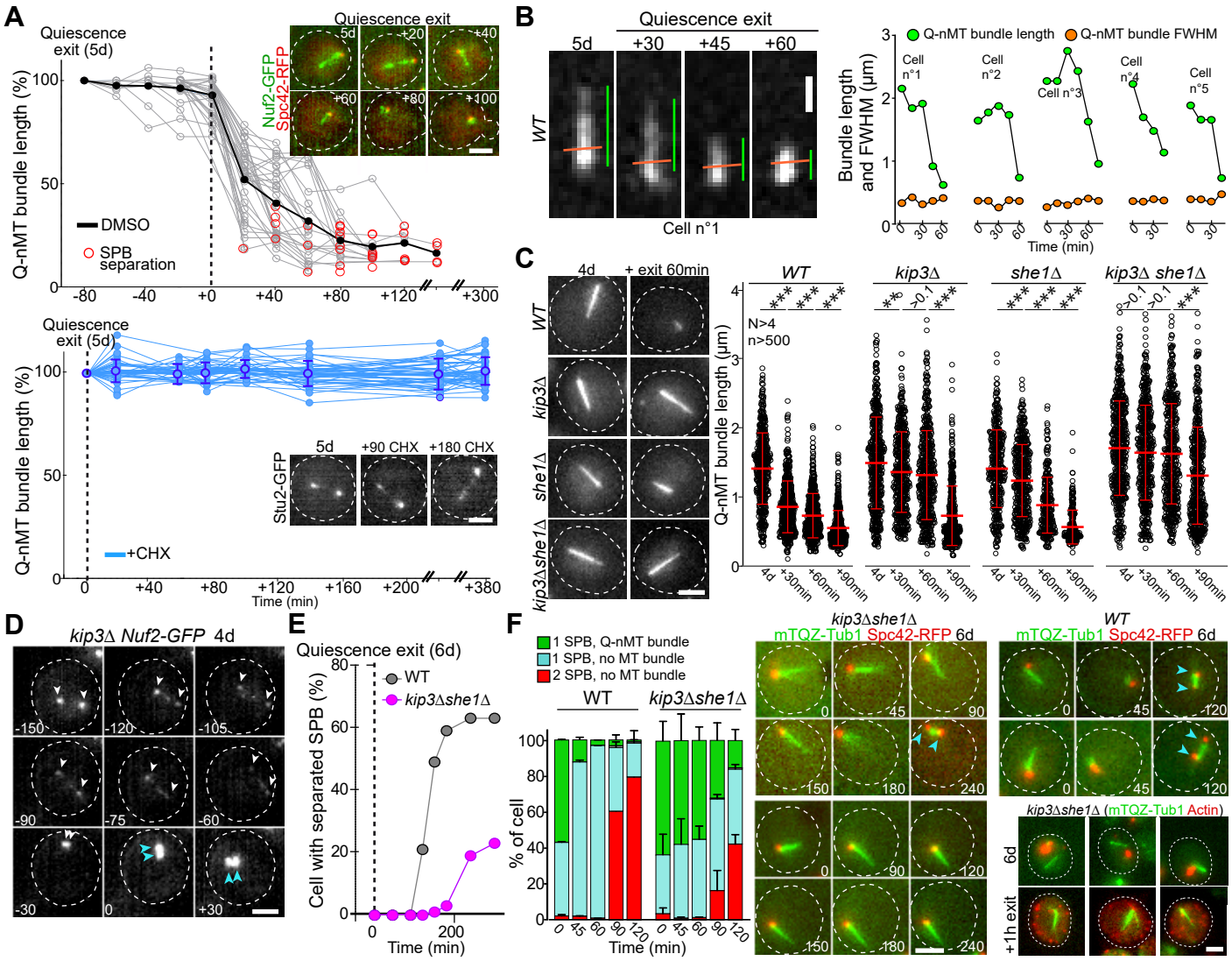
A
Quiescence exit (5d)
Q-nMT bundle length (%)
DMSO
SPB separation
Quiescence exit
Nuf2-GFP Spc42-RFP
5d
+20
+40
+60
+80
+100
+CHX
Stu2-GFP
+90 CHX
+180 CHX
Time (min)
B
Quiescence exit
5d
+30
+45
+60
WT
Cell n°1
Q-nMT bundle length
Q-nMT bundle FWHM
Bundle length and FWHM (µm)
Cell n°1
Cell n°2
Cell n°3
Cell n°4
Cell n°5
C
4d
+ exit 60min
WT
kip3Δ
she1Δ
kip3Δ she1Δ
Q-nMT bundle length (µm)
N>4
n>500
4d
+30min
+60min
+90min
D
kip3Δ Nuf2-GFP 4d
E
Quiescence exit (6d)
Cell with separated SPB (%)
WT
kip3Δshe1Δ
Time (min)
F
1 SPB, Q-nMT bundle
1 SPB, no MT bundle
2 SPB, no MT bundle
% of cell
Time (min)
kip3Δshe1Δ
mTQZ-Tub1 Spc42-RFP 6d
WT
mTQZ-Tub1 Spc42-RFP 6d
kip3Δshe1Δ (mTQZ-Tub1 Actin)
6d
+1h exit

Figure 5

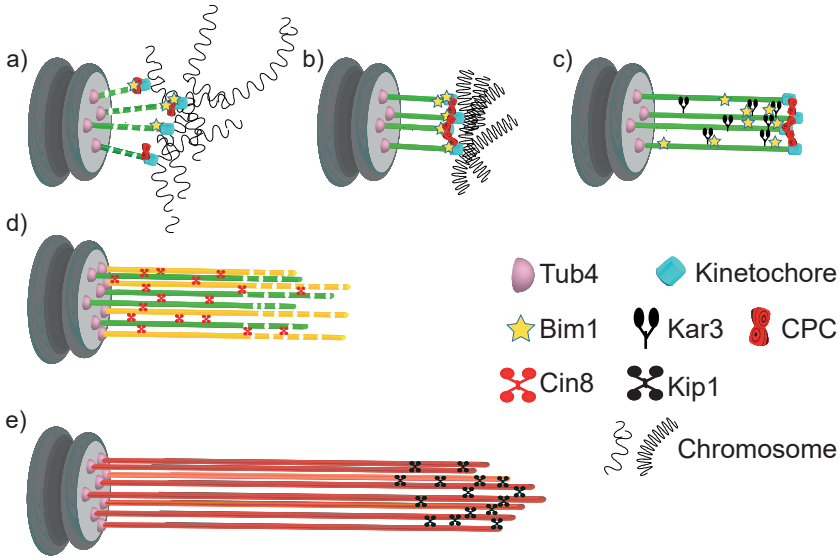

Figure 6